1-16-2002

The QMAP and MAT/TOCO Experiments for Measuring Anisotropy in the Cosmic Microwave Background

A. Miller
Princeton University

J. Beach
Princeton University

S. Bradley
Princeton University

R. Caldwell
Dartmouth College

H. Chapman
University of Pennsylvania

See next page for additional authors

THE ASTROPHYSICAL JOURNAL SUPPLEMENT SERIES, 140:115–141, 2002 June

THE QMAP AND MAT/TOCO EXPERIMENTS FOR MEASURING ANISOTROPY IN THE COSMIC MICROWAVE BACKGROUND

A. MILLER,[1,2,3] J. BEACH,[1,4] S. BRADLEY,[1] R. CALDWELL,[1,5,6] H. CHAPMAN,[5] M. J. DEVLIN,[5,7] W. B. DORWART,[1] T. HERBIG,[1,2,8] D. JONES,[5] G. MONNELLY,[1,9] C. B. NETTERFIELD,[1,10] M. NOLTA,[1] L. A. PAGE,[1] J. PUCHALLA,[5,11] T. ROBERTSON,[1,12] E. TORBET,[1,13] H. T. TRAN,[1] AND W. E. VINJE[1,14]

Received 2001 July 24; accepted 2002 January 16

ABSTRACT

We describe two related experiments that measured the anisotropy in the cosmic microwave background (CMB). QMAP was a balloon-borne telescope that flew twice in 1996, collecting data on degree angular scales with an array of six high electron mobility transistor-based amplifiers (HEMTs). QMAP used an interlocking scan strategy to directly produce high signal-to-noise ratio CMB maps over a limited region of sky. The QMAP gondola was then refitted for ground-based work as the MAT/TOCO experiment. Observations were made from 5200 m on Cerro Toco in Northern Chile in 1997 and 1998 using time domain beam synthesis. MAT/TOCO measured the rise and fall of the CMB angular spectrum, thereby localizing the position of the first peak to $l_{\rm peak} = 216 \pm 14$. In addition to describing the instruments, we discuss the data selection methods, check for systematic errors, and compare the MAT/TOCO results to those from recent experiments. The previously reported data are updated to account for a small calibration shift and corrected to account for a small contribution from known sources of foreground emission. The resulting amplitude of the first peak for $160 < l < 240$ is $\delta T_{\rm peak} = 80.9 \pm 3.4 \pm 5.1$ μK, where the first uncertainty is statistical and the second is from calibration.

Subject headings: cosmic microwave background — instrumentation: miscellaneous

On-line material: color figures

1. INTRODUCTION

Experiments aimed at measuring the anisotropy in the cosmic microwave background (CMB) require a combination of sensitive detectors and novel observing strategies. The observational goal is to measure μK celestial variations in thermal emission with a telescope observing from an environment that is some 10 million times hotter. Below 90 GHz, the detectors of choice have been high electron mobility transistor-based amplifiers (HEMTs) designed at the National Radio Astronomy Observatory (NRAO) (Pospieszalski 1992). Above 90 GHz, bolometers are the best detectors (e.g., Bock et al. 1998; Lee et al. 1996; Downey et al. 1984; Tucker 1991). SIS-based systems (Kerr et al. 1993) near 100 GHz have the speed and intrinsic sensitivity of transistor amplifiers but do not yet have the large instantaneous bandwidth of bolometers or HEMTs. Over the past 5 years, instruments have been designed for direct mapping of the CMB (e.g., QMAP, BOOMERanG, Piacentini et al. 2002; MAXIMA, Hanany et al. 2000; the TopHat experiment[15]) and for beam synthesis (Saskatoon [SK], Wollack et al. 1997; MSAM, Fixsen et al. 1996; Tenerife/Bolo, Romeo et al. 2001; PYTHON, Coble et al. 1999; VIPER, Peterson et al. 2000). More recently, interferometers based on HEMT amplifiers have reported CMB anisotropy results (CAT, Baker et al. 1999; DASI, Leitch et al. 2002; IAC, Harrison et al. 2000; CBI, Padin et al. 2001). Though the primary data product of the interferometers and beam synthesis experiments is the angular spectrum, data taken with these techniques can be turned into maps (e.g., Tegmark 1997; Tegmark et al. 1997). Conversely, there is always some filtering involved in the mapping experiments. A common element of these experiments is that they are limited by systematic error.

In this paper, the instruments for the QMAP experiment and the Mobile Anisotropy Telescope on Cerro Toco (MAT/TOCO, or TOCO for short) are described. The details necessary for assessing the quality of the data and reproducing the experimental method are also supplied. QMAP is described in part by Devlin et al. (1998), and analyses of the data are presented by Herbig et al. (1998), de Oliveira–Costa et al. (1998a, 1999), Xu et al. (2000), and Park et al. (2001). Balloon-borne mapping experiments have a long history (Weiss 1980; Partridge 1995), though highly interlocking scan strategies over limited regions of sky are

[1] Department of Physics, Princeton University, Jadwin Hall, P.O. Box 708, Princeton, NJ 08544.
[2] Hubble Fellow.
[3] Department of Astronomy and Astrophysics, The University of Chicago, 5640 South Ellis Avenue, Chicago, IL 60637.
[4] Xerox Corporation, Palo Alto, CA 94304.
[5] Department of Physics and Astronomy, University of Pennsylvania, 209 South 33d Street, Philadelphia, PA 19104.
[6] Department of Physics, 6127 Wilder Lab, Dartmouth College, Dartmouth, NH 03755.
[7] Sloan Fellow.
[8] McKinsey & Co., 3 Landmark Square, Stamford, CT 06901.
[9] Center for Space Research, Massachusetts Institute of Technology, Building 37-524, 70 Vassar Street, Cambridge, MA 02139.
[10] Department of Astronomy, University of Toronto, St. George Campus, 60 St. George Street, Toronto, ON M5S 1A7, Canada.
[11] Department of Molecular Biology, Princeton University, Princeton, NJ 08544.
[12] Department of Physics, University of California, Berkeley, 366 LeConte Hall, Berkeley, CA 94720.
[13] Department of Physics, University of California, Santa Barbara, CA 93106.
[14] Neurobiology Program, University of California, Berkeley, CA 94720.

[15] See http://topweb.gsfc.nasa.gov/index.html.

more recent (Staren et al. 2000; de Bernardis et al. 2000; Lee et al. 2001). QMAP, which flew twice in 1996, was the first of these to produce a "true map" of the CMB, complete with prewhitening and full covariance matrices. QMAP was comprised of a focal plane array of three dual polarized HEMT channels with an angular resolution of roughly 0.°8. The beam array was steered on the sky by a large chopping flat.

TOCO used the QMAP gondola and receiver refit to work with a mechanical cooler instead of liquid cryogens. It also employed two SIS-based[16] 144 GHz detector systems to improve the resolution to 0.°2. TOCO employed the SK-style beam synthesis strategy (Netterfield et al. 1995) with eight independent detectors. Instead of observing near the north celestial pole from Saskatoon, Canada, observations were made near the south celestial pole from the side of Cerro Toco in Northern Chile.[17] At 144 GHz, the atmospheric column density in Saskatoon is too large for anisotropy measurements; a high-altitude site such as the Chilean Altiplano is required. TOCO operated for two seasons in 1997 and 1998. The primary results and short description of the instrument are given by Torbet et al. (1999) and Miller et al. (1999). The 0.°2 resolution allowed us to locate the first peak in the angular spectrum. TOCO was the first experiment to do this. In the context of the popular adiabatic cold dark matter (CDM) models, this shows that the universe is geometrically flat (Doroshkevich, Zeldovich, & Sunyaev 1978; Kamionkowski et al. 1994; Bond et al. 1994; Cornish 2001).

2. OVERVIEW OF GONDOLA AND MOBILE ANISOTROPY TELESCOPE

The TOCO experiment is shown schematically in Figure 1. The part of the figure containing the optics and receiver is the QMAP balloon gondola. The radar trailer has a separable magnesium base with a 1.4 m diameter precision bearing on which the QMAP gondola is mounted. The azimuth is instrumented with an absolute 17 bit encoder and a 20 bit resolver.

[16] SIS stands for superconductor-insulator-superconductor. The detecting element is a quasi-particle mixer (Tucker & Feldman 1985).

[17] The Cerro Toco site of the Universidad Católica de Chile was made available through the generosity of Hernán Quintana, Department of Astronomy and Astrophysics. It is near the ALMA site.

3. THE RECEIVER

Radiation from the sky enters the dewar through a 15.25 cm diameter vacuum window made of 0.56 mm polypropylene and is collected with corrugated feed horns as shown in Figure 2. Three aluminum baffles define the entrance aperture: one is attached to the 40 K cold plate, one is attached to the dewar just inside the vacuum window, and one is attached outside of the dewar. Strips of aluminized Mylar connecting the cold feeds to the ambient temperature dewar block radio frequency (RF) interference and reduce optical loading on the cold stage. To prevent the formation of frost on the window, warm air is blown in front of the vacuum window.

Two NRAO SIS mixers are attached to the ≈4.5 K stage of the dewar, and six HEMTs are attached to the 40 K stage, two with center frequencies of 31 GHz (in Ka band) and four with center frequencies of 42 GHz (in Q band). Warm amplifiers, bandpass filters, noise sources, and the local oscillator for the SIS system are housed in a 293 K "backpack" attached to the outside of the dewar. The primary difference between the TOCO and QMAP receiver configurations is that QMAP used liquid cryogens and TOCO used a mechanical refrigerator to cool the HEMTs as well as the SIS mixers.

3.1. *The SIS Configuration*

The SIS configuration is shown in Figure 3. The mixers are coupled to the sky with conical corrugated feed horns. A round-to-rectangular transition at the base of the horn transforms the incoming signal to a single polarization that is added to a signal from the local oscillator using a 20 dB

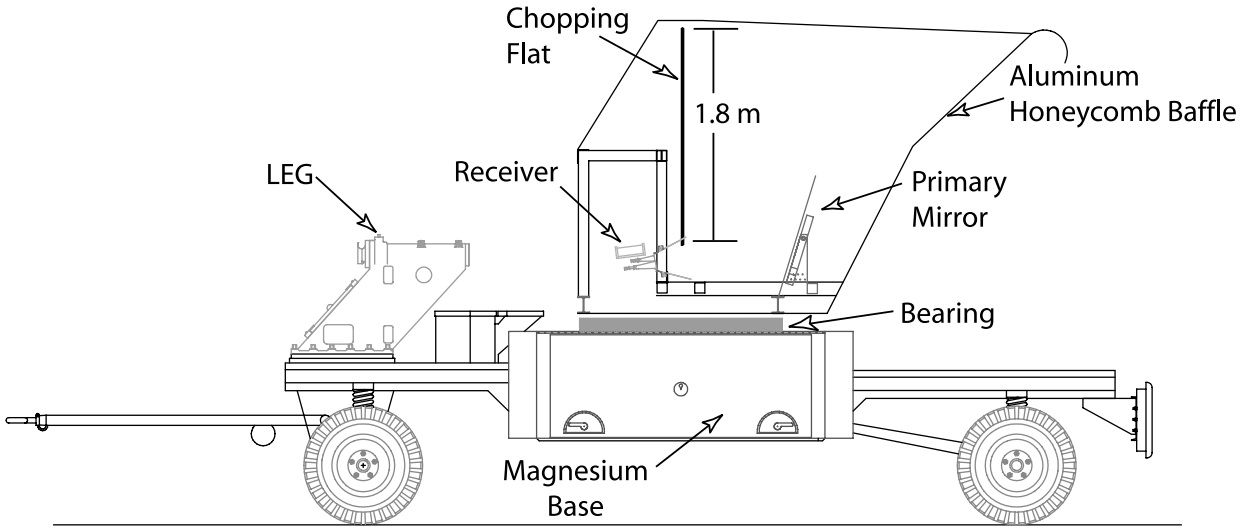

FIG. 1.—Schematic of the MAT. For transport, the legs are stowed on the left end of the trailer as shown. While observing, three legs hold the magnesium base off the trailer. The QMAP gondola is rotated using an on-axis DC motor (Compumotor DR 1100A-100 Nm torque). The motor has a 15 cm diameter hole in the center through which cables and refrigerator hoses pass from the inside of the telescope to the outside. The compressor that runs the mechanical cryocooler is mounted on the left end of the trailer while observing. [*See the electronic edition of the Journal for a color version of this figure.*]

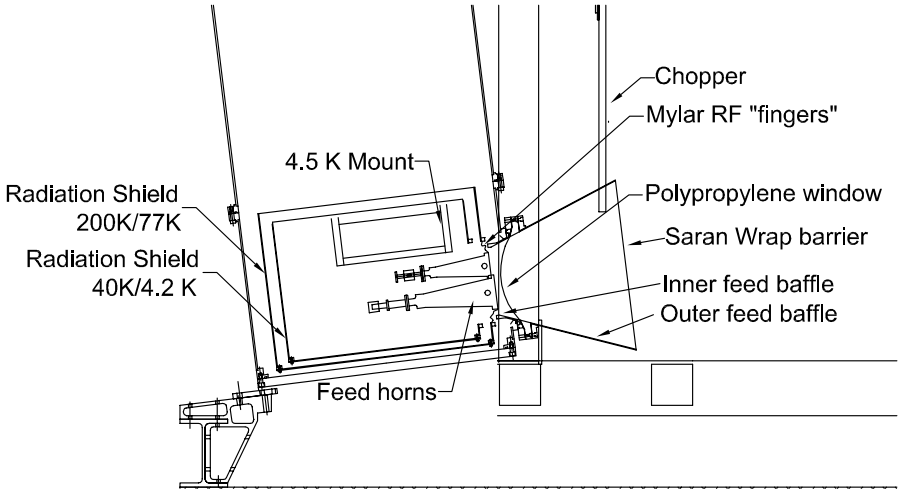

FIG. 2.—Schematic of receiver input. Shown are the 4.5 K mounting structure, the thermal shield and cold plate at 40 K, and the shield at ≈200 K. Where two temperatures are given, the first is for TOCO and the second is for QMAP. (In the QMAP configuration, the entire cold plate was cooled in the laboratory to 4.2 K with liquid helium, or to ≈2.7 K in flight at 33,000 m altitude.) The SIS mixers are mounted to the 4.5 K structure. There is a small section removed from the bottom of the chopper to accommodate the outer feed baffle. One source of modulated radiation is the cavity formed by the moving chopper and the feed baffle. Saran wrap covers the entrance of the outer feed baffle.

branch line coupler. The combined signals are fed into the SIS mixer block. A sliding backshort, connected to the outside of the dewar by a flexible shaft, is used to tune the SIS mixer, while cold, for optimal coupling. The SIS is biased through a bias T, which allows transmission of the RF signal while blocking the DC bias voltage. An associated circuit controls and reads the current through and voltage across the SIS. The signal then comes out of the bias T and goes through a 20 dB 4–6 GHz isolator (P & H Laboratories) and into a cold C-band (3.95–5.85 GHz) HEMT amplifier with 33 dB gain, as diagrammed in Figure 3. The SIS, branch line coupler, bias T, and C-band HEMT amplifier were all designed and fabricated at NRAO.

The output of the cold HEMT is carried on stainless steel semirigid coax from the cold stage to the backpack where it is amplified by a warm 44 dB RF amplifier, filtered through a 3.5–6.5 GHz filter, and detected with a detector diode (Hewlett-Packard: ±0.2 dB flatness and a typical sensitivity of 300 mV mW^{-1}). To increase the linearity and to bring the detector output into a convenient range (≈0.01 V), the diode is shunted with an ≈1 kΩ resistor. The RF filter ensures that only RF radiation in the passband of the C-band intermediate frequency (IF) amplifier makes it through the system. The detected output is then amplified by 100 and sent to the data acquisition system. The IF system temperature was measured in the laboratory with a heatable 50 Ω load and found to be $T_{\rm sys}({\rm IF}) < 6$ K. The net gain of the system is 73 dB.

The local oscillator (LO) (Millimeter Wave Oscillator Company) consists of a cavity stabilized oscillator system with an output frequency of 144 GHz. This signal goes through an attenuator and a 3 dB directional coupler and is carried by WR-6 waveguide to the cold stage. On the cold stage a 90° hybrid splits the LO power and sends it to the two mixers. The third port of the coupler is used to couple test and calibration signals into the system. The total LO power is about 8.5 mW, ≈300 nW of which impinges on each SIS mixer.

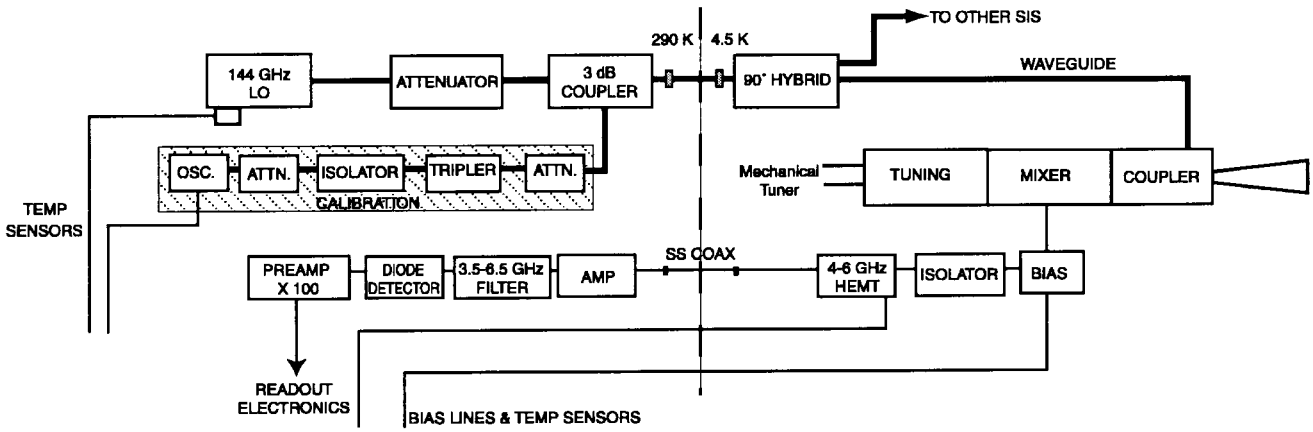

FIG. 3.—Components of the SIS receiver. The components on the right are in the dewar. Components on the left are housed in the thermally stabilized 293 K backpack. The temperatures of all critical components are monitored.

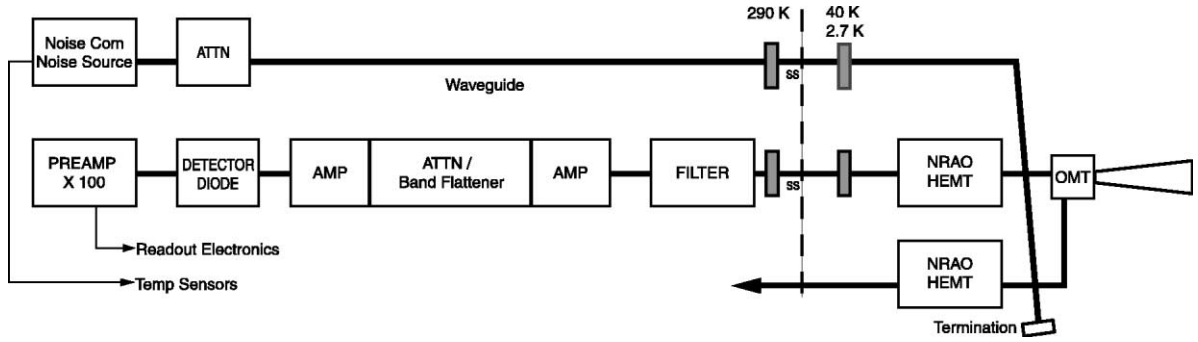

FIG. 4.—Components of a Q-band receiver, one of six HEMT radiometer channels. Components on the right are mounted to the 40 K (for TOCO, 2.7 K for QMAP) plate inside the dewar, and components on the left are in the 293 K backpack. The HEMT output is carried on a rectangular copper waveguide to the edge of the cold stage where it is connected to a 0.5 m long thin-walled stainless steel waveguide that runs down the vacuum chamber inside the dewar to warm stage. The stainless steel waveguide provides thermal isolation between the cold stage and ambient temperature. Copper waveguide from the ambient temperature end of the stainless steel segment runs to the vacuum seal, which is formed with a piece of 0.013 mm thick Kapton tape.

3.2. *The HEMT Configuration*

Figure 4 shows the configuration of the HEMT receivers for the TOCO 1997 and 1998 observing seasons. The QMAP configuration is almost identical. The radiation enters the dewar through the vacuum aperture described above and is collected using Ka- and Q-band corrugated horns. An orthomode transducer (OMT) splits the radiation into vertical and horizontal linear polarizations. The Ka-band OMT has a reflection coefficient of less than −26 dB over the bandpass of the channel. The Q-band OMTs have a reflection coefficient of less than −20 dB. Each polarization is carried by rectangular copper waveguide to a separate low-noise NRAO cryogenic HEMT amplifier (Pospieszalski 1992, 1997; Pospieszalski et al. 1994). The passband of the system is set by the amplifiers and waveguide cutoff at the low end and a filter at the high end. Bends in the waveguide are limited to a radius of curvature of at least 1.5 cm in order to minimize reflections (Monnelly 1996).

At the input to each HEMT amplifier is a 20 dB crossed-guide Bethe hole coupler that is used to inject a noise pulse. There is one source for all four of the Q-band channels and one for both Ka-band channels.

Upon leaving the dewar, each of the Ka-band signals travels through waveguide to a warm amplifier. Ka2, the vertically polarized channel (Table 1), is amplified with a single warm amplifier with 50 dB of gain and a noise figure of 3–4 dB ($T_{\rm sys} \approx 400$ K). The signal from Ka1, the horizontally polarized channel, passed through an amplifier (29 dB), an attenuator (−12 dB), and a second amplifier (also with 29 dB) before being detected with a diode. The net gain of the Ka receiver chains is ≈72 dB.

The Q-band signals, upon leaving the dewar, are carried via copper rectangular waveguide to 1 dB insertion loss filters (Spacek) that filter out the low-frequency tail of the 60 GHz atmospheric oxygen line. Following the filters the signal is amplified, sent through a band leveler (designed individually for each channel by Pacific Millimeter), and amplified again. The amplifiers are connected to the band leveler with a K connector to waveguide transition. Each amplifier has a gain of 26–28 dB and a noise figure of ≈4.5 dB. Tests of the system with and without the band levelers

TABLE 1

CENTER FREQUENCY AND NOISE BANDWIDTHS FOR EACH CAMPAIGN

	QMAP		TOCO97		TOCO98	
BAND	ν_c (GHz)	$\Delta\nu$ (GHz)	ν_c (GHz)	$\Delta\nu$ (GHz)	ν_c (GHz)	$\Delta\nu$[a] (GHz)
Ka1	32.1 ± 0.3	4.7 ± 2.2	31.7 ± 0.3	4.7 ± 2.2	...	4.7*
Ka2	30.9 ± 0.2	6.2 ± 0.3	30.8 ± 0.2	6.2 ± 0.3	32.0 ± 0.1	8.8 ± 0.1
Q1	41.4 ± 0.2	6.9 ± 0.3	41.6 ± 0.2	6.9 ± 0.3	...	6.9*
Q2	41.3 ± 0.2	7.5 ± 0.3	41.4 ± 0.2	7.3 ± 0.3	...	7.3*
Q3	42.1 ± 0.2	6.3 ± 0.3	42.2 ± 0.2	6.3 ± 0.3	42.0 ± 0.1	5.3 ± 0.1
Q4	41.2 ± 0.2	7.0 ± 0.3	41.6 ± 0.2	4.6 ± 0.3	41.7 ± 0.1	4.5 ± 0.1
D1 (USB)[b]	...	...	149.2 ± 0.2	2.9 ± 0.2	148.7 ± 0.1	2.3 ± 0.1
D1 (LSB)	...	...	138.3 ± 0.2	3.2 ± 0.2	139.5 ± 0.1	2.6 ± 0.1
D1 (DSB)	...	...	141.8 ± 0.7	5.6 ± 0.4 (3.1)	143.9 ± 0.1	4.9 ± 0.1 (2.5)
D2 (USB)	...	...	148.7 ± 0.7	2.5 ± 0.4	148.6 ± 0.1	2.4 ± 0.1
D2 (LSB)	...	...	138.9 ± 0.7	1.7 ± 0.4	139.4 ± 0.1	2.8 ± 0.1
D2 (DSB)	...	...	145.4 ± 3.0	3.6 ± 1.3 (2.1)	143.5 ± 0.4	5.2 ± 0.1 (2.6)

[a] The asterisk indicates that the bandwidth is assumed from the previous year.

[b] The D-band channels were not used in QMAP, so no value is given. The SIS bandpasses were remeasured between 1997 and 1998 because they change with SIS tuning. The numbers in parentheses following the full RF bandwidths are the effective IF bandwidths for noise calculations.

are discussed in Monnelly (1996). The net gain of each Q-band system is ≈75 dB.

A diode detector (Millitech) at the output of the final amplification stage of the HEMT channels converts the incident power to a voltage. The diode sensitivity varies over the passband and with temperature but is typically 2000 mV mW^{-1}. The output of the diode is connected to a low-noise preamplifier with a typical gain of 100 and roughly 2 kΩ input impedance. The DC output is tuned by selecting this impedance. Values vary by about a factor of 100 between different channels. The output of the preamp is buffered and sent to the data acquisition system.

3.3. *Thermal, Mechanical, and Magnetic Considerations*

In the QMAP configuration, the HEMT amplifiers and the SIS mixers are heat sunk to a cold plate that forms the bottom of the liquid helium reservoir. The outer tank of the dewar is filled with liquid nitrogen. The vapor pressures of both the nitrogen and helium are held at a constant value with mechanical regulators. The combination of pressure-regulated cryogens and a balloon-borne dewar produces a constant-temperature cold plate with minimal microphonics.

Because of the expense and difficulty of transporting liquid cryogens to Cerro Toco, the TOCO receiver is cooled with a Sumitomo cryogenic refrigerator (SRDK-408BA). The 40 K stage has 40 W of cooling power. The loading on the 40 K stage is dominated by HEMT light-emitting diodes (LEDs), waveguide connections between the cold and warm stages, and optical loading through the window. From the liquid cryogen boil-off rate in the QMAP configuration, we determined that the total loading on this stage is ≈20 W. The total loading on the 4 K stage, where there is 1 W of cooling power, is ≈400 mW.

In Chile, diurnal variations in the optical loading led to variations in the temperature of the SIS mixers of ≈400 mK. However, for the purposes of CMB anisotropy analysis, only data taken during the night when the temperatures were stable to better than 50 mK are used. The temperatures were monitored continuously and the small drifts accounted for in the analysis through a calibration model. There was also a 10 mK variation that was synchronous with the refrigerator drive motor that operates at 1.2 Hz. This term is asynchronous with the chopping frequency, and the resulting gain fluctuations are too small to affect our results (§ 13).

The backpack that houses the warm electronics mounts on the dewar and is thermally controlled to within ±0.5 K over a typical night of observations. As with the cold stage, the temperature is monitored continuously and the effects of drifts on gain are corrected in software. All microwave amplifiers are heat sunk to a common aluminum plate and their temperatures are monitored.

The enclosure for the electronics has two levels of RF shielding and is filled with pieces of microwave absorber wrapped in plastic bags that serve the dual purpose of thermal insulator and absorber of stray microwave radiation (perhaps from imperfect joints). All waveguide joints are wrapped with an absorber to prevent leakage of radiation into the rest of the system. No evidence for correlations between channels due to the instrument was found.

If changes in RF impedance due to vibrations are synchronously modulated by the motion of the chopping mirror, the resulting microphonic lines can mimic a celestial signal. Such "microphonics" can couple into the data, for example, through motion of the feeds or through strain in the microwave joints. If the coupling is large and variable, it can also affect the data even if it is asynchronous with the chopper.

In order to minimize this coupling, the cold head motor is vibrationally isolated from the dewar (which is bolted to the gondola frame) with a set of compensating flexible vacuum bellows. Bags of no. 9 lead shot are also placed on the cold head to damp vibrations. The connections between the cold head and the cooled electronics are made with strips of high purity flexible copper braid that efficiently conducts heat and vibrationally isolates the detectors from the refrigerator head.

Although microphonic levels were low at the beginning of the 1997 season, a microphonic coupling developed over the campaign that rendered the D-band data unusable for CMB observations. The coupling was manifest as 1.2 Hz (the cold head cycle) wings of a broad 90 Hz line suggesting amplitude modulation of a 90 Hz vibrational line. The source of the vibration was traced to a combination of the azimuthal drive motor and the chopper. It was corrected for the 1998 season by modifying these two systems. The electronic interference from the azimuthal drive motor was eliminated by installing a brake. The brake allows the motor to be shut off during CMB observations and prevents large currents from being drawn by the motor working to counteract wind loading. In addition, the chopper-induced vibrations were reduced by replacing the bearings in the chopper with flex pivots. As a result, microphonic levels in the TOCO98 D-band data were negligible. Microphonics were not a problem either year in the HEMT data.

The Josephson junctions in the SIS mixers are sensitive to magnetic fields. Helmholz coils placed around the dewar were used to measure the dependence. With the coils absent, the area was mapped with a Gauss meter to ensure that the AC fields from the chopper drive and cold head motor would not contaminate the data. To minimize potential magnetic coupling, high magnetic permeability material (mu-metal) was wrapped around the outside of the chopper coils and around the cold head. Not only is the magnetic field negligible, but the chopper-synchronous component corresponds to values of l that do not enter into the CMB analysis.

3.4. *Receiver Characteristics*

The QMAP/TOCO receiver was characterized in the laboratory before each campaign, but the most relevant characterizations are done while observing. We use the following definitions:

$$\nu_c = \frac{\int \nu A(\nu) g(\nu) d\nu}{\int A(\nu) g(\nu) d\nu}\ , \quad \Delta_n \nu = \frac{\left[\int g(\nu) d\nu\right]^2}{\int g^2(\nu) d\nu}\ , \qquad (1)$$

where A is the atmospheric transmission function, g is the receiver passband, ν_c is the effective center frequency, and $\Delta_n \nu$ is the noise bandwidth (Dicke 1946) for the radiometer equation.[18]

[18] Throughout the paper, ν is for RFs and f is for audio (<20 kHz) frequencies. Including the atmosphere for TOCO shifts the centroids between 0.1 and 0.5 GHz higher than for the QMAP values.

The noise of HEMT-based amplifiers has a $1/f$ characteristic (Jarosik 1996; Wollack 1995). To parameterize it, the power spectrum of the detector diode output is fitted to the following form:

$$\tilde{T} = T_{\rm sys}\sqrt{\frac{1}{\tau\Delta_n\nu}+f^{\alpha}} = T_{\rm sys}\sqrt{\frac{1}{\tau\Delta_n\nu}+\left[\frac{\Delta G(f)}{G}\right]^2}, \quad (2)$$

where $\tilde{T}$ is the system sensitivity in units of K $s^{1/2}$, τ is the integration time, and $\Delta G/G$ is the fractional gain fluctuation that gives rise to the $1/f$ form. When the bandwidth is very large, the gain fluctuations dominate as shown by Wollack & Pospieszalski (1998). Note that a $1/f$ noise spectrum corresponds to $\alpha = -1$ in the variance ("power") of the detector output. The $1/f$ knee, $f_{\rm knee}$, is where the frequency of the power spectrum (square of eq. [2]) increases by a factor of 2 over the value at high frequencies.

The instrument bandpasses, $g(\nu)$, are measured in the laboratory for each channel. Table 1 lists the center frequencies and effective noise bandwidths for each channel for each observing campaign as calculated from equation (1).

The SIS is operated in double sideband (DSB) mode. By convention we use the IF noise bandwidth in the radiometer equation and report "double sideband noise temperatures," $T_{\rm DSB}$, because our source fills both RF bands. If a source fills just one RF band, a "single sideband noise," $T_{\rm SSB}$, is reported. In an ideal system, $T_{\rm DSB} = T_{\rm SSB}/2$. We use the mean of the upper sideband (USB) and lower sideband (LSB) bandwidths for the noise bandwidth in the radiometer equation. A full calculation of the noise includes contributions from the mixer and the IF amplifier (Blundell, Miller, & Gundlach 1992; Kerr, Feldman, & Pan 1997); for our purposes we treat these as lumped elements.

3.4.1. *SIS Sensitivity*

Measurements of the SIS sensitivity have been made in several configurations as shown in Table 2. The values of $T_{\rm rec}$ from laboratory measurements are better than those made in the field. To investigate this discrepancy, an external cold load that bolts onto the front of the receiver to mimic the sky was built. It was possible to approximately reproduce the system temperatures measured with the internal load using an external load provided that the tuning parameters were readjusted. This retuning compensates primarily for the change in temperature of the mixer. In the 1998 season, the combination of thermal loading and increasingly poor refrigerator performance led to an increase in the SIS temperatures and a temperature distribution different to that in the laboratory. Even though the system was tuned in the field, the laboratory performance was not duplicated.

The SIS system noise exhibits a $1/f$ characteristic presumably due to the C-band HEMT, though this has not been verified. The $1/f$ noise is parameterized following equation (2) in the last two lines of Table 2.

TABLE 2
SIS System Parameters

Parameter	D1 (Laboratory)	D1 (Field)	D2 (Laboratory)	D2 (Field)
$T_{\rm phys}$[a] (K)	4.3	4.9	4.4	4.9
V_B[b] (mV)	13.4	13.8	14.2	14.6
$\tilde{T}_{\rm DSB}$[c] (mK $s^{1/2}$)	0.6	1.3	0.7	1.2
$T_{\rm sys}$[d]	30	65	...	61
$T_{\rm rec}$[e]	26	48	...	44
$T_{\rm rec}$(y-factor)[f]	27	...	35	...
α	...	−1.0	...	−0.8
$f_{\rm knee}$ (Hz)	...	18	...	12

[a] The physical temperature of the SIS body. The uncertainty is approximately ±0.2 K. At $T > 5$ K the SIS sensitivity is markedly reduced.
[b] The optimal SIS bias voltage, V_B, across the six SIS junctions.
[c] The total power DSB sensitivity computed from the noise power spectrum at 200 Hz, where atmospheric fluctuations are negligible, and the responsivity. These are for a Rayleigh-Jeans source. In the field, the atmosphere and telescope contribute ≈17 K. In the laboratory, the load contributes ≈4 K. The loss from the feeds is measured to be negligible.
[d] The Rayleigh-Jeans system temperature computed from measured sensitivity and the noise bandwidth, $T_{\rm sys} = \tilde{T}(\Delta\nu)^{1/2}$.
[e] The Rayleigh-Jeans receiver temperature computed from $T_{\rm sys}$.
[f] The Rayleigh-Jeans receiver temperature measured with a variable temperature cryogenic load.

3.4.2. *HEMT Sensitivity*

The same set of six HEMT amplifiers was used for the two QMAP flights and the two observing seasons of the TOCO experiment; four of these six were used for the SK measurement. They were tested in the laboratory before each set of observations and the sensitivities were analyzed for each data set (Table 3). There is evidence of degradation in the HEMT performance between the QMAP and TOCO campaigns above that which is expected as a result of the difference in body temperature (Pospieszalski 1989). Generally, HEMT system noise is expected to increase roughly 1 K for each kelvin of increased ambient temperature. We suspect slow deterioration in the mechanics of the microwave/bias structures over the hundreds of cycles and sometimes rough handling these amplifiers experienced. The chips were produced from unpassivated InP, so there may have been some deterioration in the chip performance, though this has not been confirmed.

4. OPTICS

The telescope optics are similar to those used in the SK experiment (Wollack et al. 1997). Corrugated feeds underilluminate a 0.86 m primary mirror, which in turn underilluminates a flat (1.8 × 1.2 m) chopping mirror (chopper). Each of the eight channels detects a single mode of a diffraction-limited beam. The chopper is a resonant, computer-controlled mirror that scans in the azimuthal direction while the rest of the optics remains fixed in azimuth and elevation as the sky rotates through the beams. The telescope sits inside an aluminum ground screen that is fixed with respect to the primary mirror, the receiver, and the chopper mount.

4.1. *The Focal Plane*

Conical corrugated feed horns receive radiation from the sky and transform the incident fields so they may propagate through waveguide. All of our feeds were fabricated by Custom Microwave from electroformed copper over an aluminum mandrel. They are gold coated to stabilize the surface. The general electromagnetic design follows the guidelines in Clarricoats & Olver (1984) and Thomas (1978). The throat section, where the corrugations adiabatically transform from $\lambda/2$ depth to $\lambda/4$ depth as the hybrid mode detaches from the feed wall, was designed by Wollack (1994) follow-

TABLE 3
HEMT Amplifier System Parameters

	QMAP[a]				TOCO97[b]		TOCO98			
Band	T_{sys} (K)	$\tilde{T}$ (mK $s^{1/2}$)	α	f_{knee} (Hz)	T_{sys} (K)	$\tilde{T}$ (mK $s^{1/2}$)	T_{sys} (K)	$\tilde{T}$ (mK $s^{1/2}$)	α	f_{knee} (Hz)
Ka1.....	22	(0.40) 0.36	−1.2	62	89	1.3	162	(2.6) 2.4	−0.90	14
Ka2.....	23	(0.42) 0.32	−0.92	141	63	0.8	59	(0.9) 0.62	−0.85	95
Q1.....	17	0.21	...	...	91	1.1	84	(1.2) 1.0	−0.84	64
Q2.....	22	(0.60) 0.25	−0.82	686	145	1.7	114	(3.3) 1.3	−1.57	168
Q3.....	155	(2.1) 2.0	−0.78	20	63	0.8	80	(0.9) 0.72	−0.84	37
Q4.....	53	(0.85) 0.64	−0.71	67	156	2.3	88	(1.6) 1.3	−0.88	42

[a] From the first QMAP flight as shown in Devlin et al. 1998. Q1 did not work during the flight, so we report the laboratory measurements (Monnelly 1996). The four entries for each campaign correspond to the system temperature, the measured system sensitivity at 100 Hz (in parentheses) and very high frequencies, the gain fluctuation exponent, and the $1/f$ knee. In the fits to the power spectra, $f < 5$ Hz is not included. Because of the $1/f$ HEMT characteristics, $\tilde{T} = T_{sys}/(\Delta_n \nu)^{1/2}$ is always smaller than the measured value of $\tilde{T}$ at 100 Hz. With the centroids in Table 1, the full noise spectrum may be recovered.

[b] From measurements in the field at 100 Hz.

ing the work of James & Thomas (1982).[19] The voltage standing wave ratio (VSWR) is less than 1.05 across the waveguide band, and the loss in the feed is negligible. The feeds are modeled with a commercial code (YRS Associates), CCORHRN, that solves for the full electromagnetic field that propagates in the feed. Table 4 summarizes parameters of the feed horns used in the QMAP and TOCO experiments.

Figure 5 shows a map of the beam pattern made by observing Jupiter. The feed horns are arranged so that the D-band beams with 0.°2 resolution are placed as close to the center of the focal plane as possible. Beam parameters for each channel have been calculated and measured for each campaign as shown in Table 5.

4.2. *Optical Components*

The primary mirror is a simple offset parabola. In the notation of Wollack et al. (1993), the offset angle is $\Psi_P = 48°$, and the focal length is 0.9 m. The dewar views the parabola at an angle of $\Psi_D = 7°$, thus the zenith angle of the optical axis is $90° - \Psi_P + \Psi_D = 49°$. The diameter of the parabola in projection is 0.86 m. The rms surface tolerance is $\approx 15\ \mu$m.

The chopper design follows that described by Wollack et al. (1997) with a few modifications. It is smaller and lighter than the SK chopper, measuring 1.8×1.2 m, and is driven at the resonant frequency of a flat steel spring plate ($85 \times 8.62 \times 0.167$ cm for TOCO98) attached at its middle to the chopper mount. The surface tolerance of the plate is $\approx 30\ \mu$m. The thickness of the spring plate is tuned for each campaign. The resonant system produces a sinusoidal sweeping pattern in azimuth that requires minimal drive power and produces minimal vibrations on the mount. There is no reaction bar on the QMAP/TOCO chopper.

The chopper position is sensed 80 times per chop with a set of redundant linear variable differential transformers (LVDTs), one on each side of the mirror. Errors in the sinusoidal chopper motion due to wind loading or instrument glitches are measured. The temperature of the chopper is monitored at all times using nine thermometers placed at various locations on the flat.

[19] In Ka band, the depths of grooves 1–10 are 0.411, 0.368, 0.351, 0.335, 0.323, 0.312, 0.302, 0.292, 0.282, and 0.274 cm. This feed was designed by Ed Wollack.

TABLE 4
Design Parameters for All Feeds

Parameter	Ka	Q1/2	Q3/4	D
Semiflare angle θ_o (deg).....	6	4.4	5.4	5.4
Skyward aperture diameter d_h(cm).....	4.2	2.0	2.1	0.89
OMT aperture diameter (cm).....	0.833	0.650	0.650	0.173
Beamwidth θ_{beam}^{FWHM} (deg)....	18	18	16	17
Phase error Δ (Thomas 1978).....	0.11	0.065	0.051	0.011
VSWR.....	1.03	1.03	1.03	1.05
Forward gain (dBi).....	20.9	20.6	21.4	20.8
Number of corrugations.....	71	67	85	82
Length (cm).....	19.3	12.0	14.5	3.96

5. OFFSETS AND SIDELOBES

Emission from the instrument produces signals that can potentially complicate the measurement.[20] These signals are generically called "offsets" as they are fairly constant over long periods and would be present in the absence of a celestial signal. Examples are shown in Figure 6. Outside of the data selection based on weather, most of the analysis effort goes into ensuring that offsets do not contaminate the final results. This section addresses the known offsets and sets upper limits on their magnitudes for the cases in which the

[20] The Sun is another source. For TOCO, the Sun travels overhead and so cannot be completely blocked at all times. However, for CMB work only data from the nighttime and early morning, when the Sun is fully blocked from the optics, are used. QMAP flew at night. Lunar emission was not seen in either experiment. For TOCO, the data were binned according to the angular distance to the Moon in Ka band, and no systematic effect was found. For QMAP the Moon is greater than 60° from the beam and thus negligible.

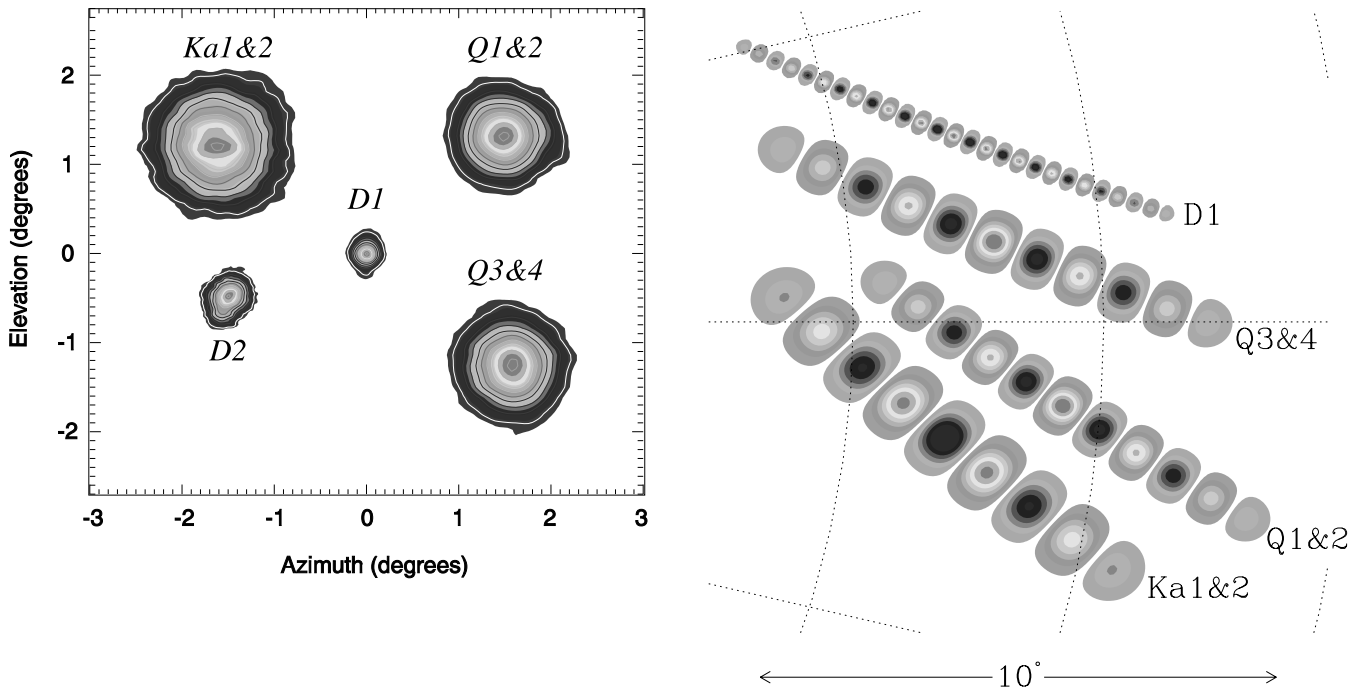

FIG. 5.—Beam map of focal plane (*left*) and the synthesized beams (*right*). *Left:* Units are degrees on the sky from the center of the focal plane. Each beam is normalized with the contours representing 10% in amplitude. The physical separation between the Ka1/2 horn and the Q1/2 feed is ≈5 cm. D2 is offset from the focal plane center by 2.9 cm. The distance between the Q1/2 and Q3/4 feeds is also ≈5 cm. This is also a picture of the up/down reflection of the feeds in the focal plane when looking into the dewar. *Right:* Synthesized beams for TOCO97 as discussed in § 10. If the Ka primary beam on the left, for example, is weighted by positive and negative numbers as it moves across the sky, one obtains the synthesized Ka pattern on the right. The contours indicate alternate positive and negative lobes. Shown are the Ka 9-pt, Q 11-pt, and D 27-pt beams. From this picture, it is clear that the synthesized beam is sensitive to only a narrow band of spatial frequencies. The central dashed line corresponds to R.A. = 0 (Fig. 8) though the synthesized beam location as shown is arbitrary. In the full analysis, the beam is smoothed in right ascension. [*See the electronic edition of the Journal for a color version of this figure.*]

source is chopper modulated (radiation that enters the detectors after being affected by the chopper) and unmodulated (radiation that enters the detectors directly). The offsets from modulated emission can, in principle, occur at any harmonic of the chopper frequency.[21] In practice, they are predominantly at the lowest spatial frequency harmonics.

In the following the focus is on TOCO because the long observing campaigns required careful monitoring of the offsets. In QMAP, because of the short durations of the flights, the offsets were stable. In the mapmaking analysis, the offsets were projected out of the CMB data using a technique described in de Oliveira–Costa et al. (1998a).

5.1. *Earth Emission Offset*

Radiation from the Earth can diffract over the front edge of the ground screen and enter the receivers. The temperature of the ground as seen by the detectors is

$$T_A \approx \frac{g_{\rm feed}(\theta)}{4\pi}\left(\frac{D^2}{r}\right) T_{\rm E}\Omega_{\rm E}\ , \qquad (3)$$

with

$$D = -\frac{\sqrt{\lambda}}{4\pi}\left\{\frac{1}{\cos[(\gamma-\alpha)/2]} \pm \frac{1}{\sin[(\gamma+\alpha)/2]}\right\}\ , \qquad (4)$$

where $T_{\rm E}$ is the physical temperature of the Earth (≈273 K); $g_{\rm feed}(\theta)$ is the gain of the feed as defined by $G_{\rm max}P_n(\theta)$, where $G_{\rm max}$ is the forward gain and $P_n(\theta)$ is the normalized beam pattern; $\Omega_{\rm E}$ is the solid angle of the Earth subtended by the telescope rim; r is the distance from the horn to the top front edge of the baffle; γ and α are the diffraction angles; and D is the diffraction coefficient (Keller 1962). The positive sign in D is for the E-field perpendicular to the edge, and the negative sign is for the E-field parallel to the edge.

From integrating equation (4) over the geometry of the ground screen and the feed pattern, we find the diffracted power in D band into the feed $T_A \approx 25\ \mu$K. The front baffle, which is in the far field of the feed, has a "Keller flare" that reduces the diffracted power over that from the sharp edge assumed in the calculation. Based on our experience, calculations of this type involving complicated geometries are accurate to roughly a factor of 3. This factor is included in Table 6 where results are summarized.

The modulated contribution is estimated the same way as above but with $g_{\rm feed}(\theta)$ replaced by $g_{\rm beam}(\theta)$, the far-field gain of the main beam rather than the gain of the horn. The calculated power diffracted into the chopper sidelobes is ≈5 μK. The front baffle is in the near field of the main beam, so the true values could be up to an order of magnitude larger. If the temperature of the ground on either side of the telescope were to differ by 10 K, then the offset produced would be less than 1 μK. Similarly, any modulation of diffracted power from variations along the top of the ground screen is small. From these estimates we conclude that emission from the Earth does not contribute to the microwave signal.

[21] We use the term "harmonic" to refer to the spatial frequencies of the scan pattern as discussed in § 10.

TABLE 5
BEAM PARAMETERS

Campaign	Ka1	Ka2	Q1	Q2	Q3	Q4	D1	D2
Predicted								
Ω_A[a] (10^{-4} sr)	2.76	2.76	1.53	1.53	1.69	1.69	0.124	...
θ^{az}_{FWHM}[b] (deg)	0.905	0.905	0.663	0.663	0.702	0.702	0.190	...
θ^{el}_{FWHM}[b] (deg)	0.888	0.888	0.661	.661	0.683	0.683	0.192	...
Polarization	↔	↕	↔	↕	↔	↕	↔	↕
Pri ET (dB)[c]	−21	−21	−19	−19	−20	−20	−22	...
Chop ET (dB)	−47	−47	−48	−48	−49	−49	−54	...
QMAP96a								
Ω_A(10^{-4} sr)	2.83	2.83	1.58	1.58	1.62	1.62	...	...
θ^{Maj}_{FWHM} (deg)	0.931	0.931	0.694	0.694	0.700	0.700	...	...
θ^{Min}_{FWHM} (deg)	0.882	0.882	0.658	0.658	0.668	0.668	...	...
Cross-El (deg)	−1.35	−1.35	1.35	1.35	1.35	1.35	...	...
QMAP96b								
Ω_A(10^{-4} sr)	2.67	2.67	1.43	1.43	1.75	1.75	...	...
θ^{Maj}_{FWHM} (deg)	0.932	0.932	0.674	0.674	0.730	0.730	...	...
θ^{Min}_{FWHM} (deg)	0.831	0.831	0.616	0.616	0.694	0.694	...	...
Cross-El (deg)	−1.35	−1.35	1.35	1.35	1.35	1.35	...	...
Elevation (deg)	41.36	41.36	41.37	41.37	38.79	38.79	...	...
TOCO97[d]								
Ω_A(10^{-4} sr)	2.76	2.73	1.63	1.74	1.76	1.78	0.183	0.323
σ_Ω[e] (%)	6	6.5	4	8	4	6.0	5	6
θ^{az}_{FWHM} (deg)	0.881	0.871	0.711	0.744	0.718	0.716	0.225	0.306
θ^{el}_{FWHM} (deg)	0.909	0.909	0.664	0.676	0.711	0.721	0.236	0.306
Azimuth (deg)	203.13	203.13	206.75	206.75	206.70	206.70	205.00	...
Elevation (deg)	41.75	41.75	41.85	41.85	39.25	39.25	40.44	39.93
TOCO98								
Ω_A (10^{-4} sr)	3.00	3.00	1.52	1.60	1.76	1.80	0.136[f]	0.292
σ_Ω (%)	8	8	9.8	18	8.4	10	5.5	5
θ^{az}_{FWHM} (deg)	0.860	0.914	0.666	0.669	0.692	0.688	0.201	0.293
θ^{el}_{FWHM} (deg)	0.907	0.918	0.659	0.681	0.732	0.754	0.194	0.286
Azimuth (deg)	205.67	205.67	209.16	209.16	209.06	209.06	207.47	205.73
Elevation (deg)	42.05	42.05	42.03	42.03	39.48	39.48	40.63	40.13

[a] Solid angle of beam.
[b] FWHM in the azimuthal and elevation direction. The beam is not symmetric as a result of smearing in the azimuth direction and the placement in the focal plane. For QMAP, the major and minor axes of the best-fit ellipsoidal Gaussian are given.
[c] The edge taper is the ratio of radiant power in the center of the optic to that on the edge expressed in dB. This is determined from a full calculation of the current distribution on each optical element using the DADRA program (YRS Associates).
[d] The chopper was tilted around its normal for TOCO97, hence the beam moved in elevation by $0.116 \sin(\theta_{\text{az-chop}})$ deg. There was no tilt in TOCO98.
[e] The rms in the fitted solid angle during the campaign rounded to the nearest 0.5%.
[f] The prediction is for the 1998 configuration. D band is also the most sensitive to slight changes in alignment.

5.2. *Ground Screen Emission Offset*

The antenna temperature from emission of the baffles as seen by the receiver is

$$T_A \approx \frac{g_{\text{feed}}(\theta)}{4\pi} \epsilon_{\text{baffle}} T_{\text{baffle}} \Omega_{\text{baffle}} \approx 5 \text{ K} , \qquad (5)$$

where ϵ_{baffle} is the emissivity of the baffle and T_{baffle} is its physical temperature. Direct emission from the ground screens and atmosphere dominates the radiation loading. As with the diffracted ground emission, one may ask what portion of this signal is modulated. We find that the temperature of the baffle in the main beam, after reflecting off the chopper, is ≈80 mK. A temperature differential of 10 K on either side of the baffle would then correspond to an observed offset of ≈1.5 mK in the lowest harmonics. It is also possible to get modulated emission because the polarization of the emission is a function of the angle of the beam with respect to the ground screen. The geometry of the enclosure is complicated, but the angle of the ground screen implies that such emission will be greatest in the vertical polarization. However, the modulation will be greatest for the horizontal component. This term is similar in character to the polarized emission from the chopper but is an order of magnitude smaller.

5.3. *Cavity Emission Offset*

The cavity behind the chopping mirror (Fig. 2) and outer feed baffle is effectively black. Radiation from this

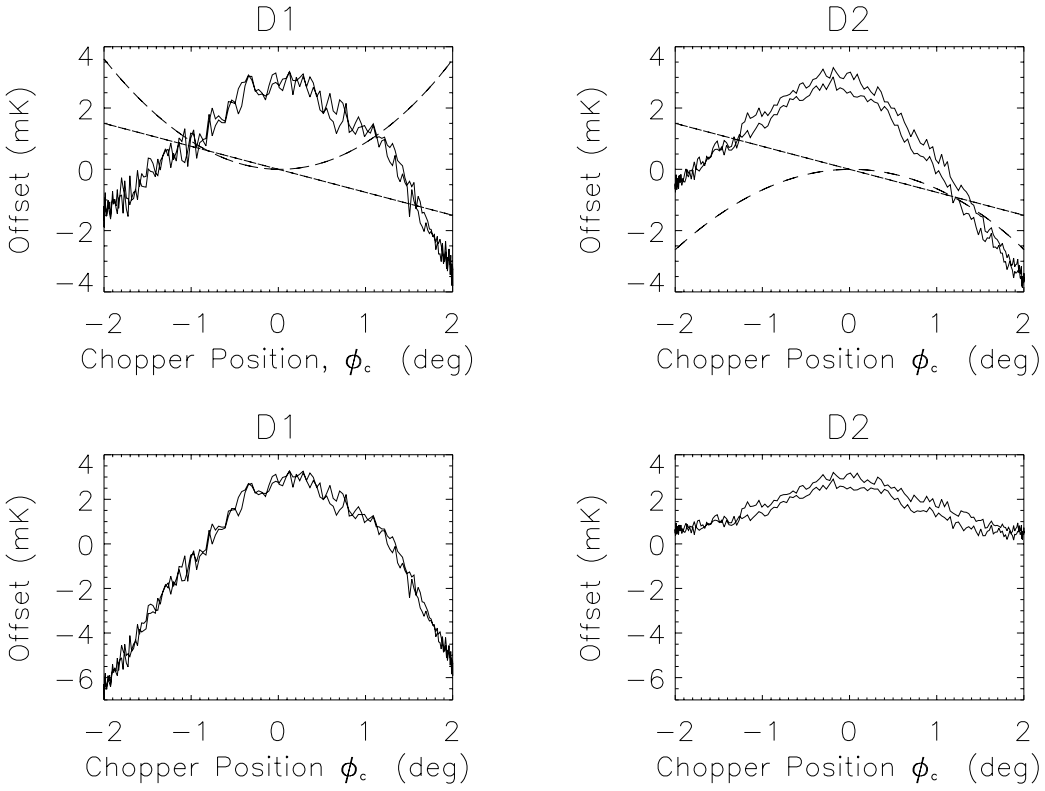

FIG. 6.—*Top panels:* Measured chopper offsets, O_i, in D band as a function of chopper position for a typical night of CMB data. This plot shows the raw data (with cal pulses subtracted) synchronously co-added with the chopper azimuth, ϕ_c. Dashed lines are the calculated offsets due to polarized emission from the chopping mirror with the offset at the center of the chop removed, $T(\phi_c) - \langle T(\phi_c = 0)\rangle$. The straight lines are the calculated offset due to a mirror tilt of $\delta\theta_{\|} = 0.^{\circ}1$ in the plane of the stationary chopper. When these offsets are multiplied by a synthesis vector, the result is constant in time and independent of chopper position. D1 is horizontally polarized; D2 is vertically polarized. *Bottom panels:* Residual measured offset after the subtraction of the predicted offsets. The form of the residual indicates that the source is polarized. The asymmetry in D1 may be due to feed rotation.

cavity reaches the receiver (1) by traveling over the front edge of the outer feed baffle and back into the feeds or (2) through shallow angle diffraction over the outer feed baffle onto the parabola and then reflecting back to the feeds. This emission is modulated as the chopping mirror sweeps back and forth, changing the size and shape of the opening to the emitting cavity. Improved shielding of this cavity between the two QMAP flights reduced the

TABLE 6
ESTIMATED CONTRIBUTIONS TO THE OFFSETS

Contributions to the Signal	D Band	Q Band	Ka Band	Modulated
Earth emission (directly into feed)[a] (μK)	75	300	400	No
Earth emission (in chopper sidelobes)[b] (μK)	<50	<200	<250	No
Ground screen emission (directly into feed) (K)	5	6	7	No
Ground screen emission (in chopper sidelobes) (mK)	80	80	80	No
Cavity emission, vertically polarized (mK)	3	13	15	No
Total loading from optics (K)	5	6	7	
Total ground screen emission[c] (mK)	1.5	1.5	1.5	Yes
Cavity emission (vertically polarized)[d] (mK)	0.3	1.3	1.5	Yes
Polarized chopper emission[e] (mK)	3.5	1.8	1.6	Yes*
$\delta T_{\|}$ mirror misalignment in atmosphere (mK)	3	1.7	1.7	Yes*
$\delta T_{\perp}$ mirror misalignment in atmosphere (μK)	20	10	10	Yes*
Feed rotation (1°) (mK)	3	0.8	0.6	Yes*
Feed rotation (4°) (mK)	10	3	2	Yes*

[a] Results of the formal calculation times 3 to account for modeling uncertainties.
[b] Includes a factor to account for near field effects.
[c] Due to a hypothetical temperature gradient across the ground screen.
[d] The effective area of the cavity between the chopper and the outer feed baffle is estimated to be modulated by 10%.
[e] Magnitude of the largest component of polarized emission. An asterisk indicates that this quantity is computed to 10% accuracy.

offset at a given angle of the chopper by 1.8 mK or 50% in Ka band (Herbig et al. 1998).

The contribution from radiation traveling over the feed baffle and back into the feeds may be estimated with equation (4). For D band, $T_A \approx 3$ mK for vertically polarized radiation and $T_A \approx 0.1$ mK for horizontally polarized radiation.

The contribution from the shallow angle diffraction is difficult to compute to even order-of-magnitude accuracy because it is so critically dependent on the geometry. This term, though, can be of mK magnitude and horizontally polarized.

5.4. *Chopper Polarized Emission Offset*

The emission from the chopping plate is polarized and depends on the angle of the mirror (Landau & Lifshitz 1960; Wollack et al. 1993; Cortiglioni 1994). Therefore, as the chopping mirror scans across the sky, the plate emissivity, as viewed by a feed, changes with the position of the chopper. The parallel and perpendicular emissivities are $\epsilon_{\|} \approx \epsilon_0/\cos\theta_i$ and $\epsilon_{\perp} \approx \epsilon_0 \cos\theta_i$, where ϵ_0 is the emissivity at normal incidence and θ_i is the incident angle of radiation that changes with chopper azimuth.

The brightness temperature of the plate is

$$T_{\rm emit} \approx T_{\rm chop}\left(\epsilon_{\|}\left|\tilde{E}_{\|}(\theta_i)\right|^2+\epsilon_{\perp}\left|\tilde{E}_{\perp}(\theta_i)\right|^2\right) , \qquad (6)$$

where $\tilde{E}_{\|}$ and $\tilde{E}_{\perp}$ are the parallel and perpendicular electric field projections onto the normal to the chopping mirror and $T_{\rm chop}$ is the physical temperature of the chopper. For the D band, the peak-to-peak calculated offset is $\approx$3.5 mK. The dashed curves in Figure 6 show the polarized emission offset calculated for each of the channels.

In the beam synthesis, the net signal for each chopper position is multiplied by the corresponding element in the synthesis vector (§ 10). The offset, since it is an additive signal, is multiplied by the same vectors. It is evident from Figure 6 that the offset in the synthesized signal, or "synthesized offset," will be larger for the smaller harmonics. The polarization directions were chosen to minimize the synthesized offset for the 3-pt beam as no science data are expected from the 2-pt beam.

5.5. *Atmospheric Offsets*

When the telescope is properly aligned, the chopper scans horizontally through the atmosphere and the atmospheric emission temperature at all portions of the chop is the same. If either the chopping mirror or the entire base is misaligned with respect to the horizontal, offsets are produced (Wollack et al. 1997) according to

$$T_{\rm atm} = \langle T_{\rm atm}\rangle + T_z \tan\theta_z \sec\theta_z\left(\delta\psi_{\|} + \delta\psi_{\perp}\right) , \qquad (7)$$

where T_z is the zenith temperature and θ_z is the fiducial zenith angle of the beam. If the chopper is misaligned as a result of a rotation about an axis parallel to the chopper normal, the sky signal is changed by

$$\delta\psi_{\|} \approx 2\delta\theta_{\|} \sin\theta_z \sin\phi_c ,$$

where ϕ_c is the azimuthal chopper angle. If the chopper is misaligned as a result of a rotation about an axis perpendicular to the chopper normal, the sky signal is changed by

$$\delta\psi_{\perp} \approx -2\delta\theta_{\perp} \cos\theta_z \cos\phi_c .$$

Measurements of chopper and base tilt put a limit on the measured value of $\delta\theta_{\|}$ and $\delta\theta_{\perp}$ of $\leq 0.^\circ 1$. Assuming this value, $\delta T_{\|} \approx 3$ mK and $\delta T_{\perp} \approx 20\ \mu$K are expected for D band.

5.6. *Observed Offset*

Figure 6 shows the chopper position–dependent offsets observed in each of the D-band channels on a typical night analyzed for CMB observations in the 1998 campaign. Plotted in the top panels are the observed offsets (in antenna temperature) as a function of azimuthal chopper angle. Overplotted are the computed polarized emission offsets for each of the channels (*dashed line*) and offset due to mirror tilt about an axis parallel to the chopper normal (*solid line*). The bottom panels show the offsets corrected for these two effects.

There is a clear asymmetry in the offset about $\phi_c = 0$ in the top panels of Figure 6. This is most likely caused by a misalignment of the chopper with $\delta\theta_{\|} = 0.^\circ 1$, corresponding to the D-band beam centroid moving up and down vertically $\delta\Psi_{\|} = 0.^\circ 0053$ as it scans the azimuth. This angle is just below the detection threshold of our measurements (§ 7). With a zenith temperature of 10 K in D band, $\delta\theta_{\|} = 0.^\circ 1$ produces a 1.6 mK modulation.

Another mechanism for producing an asymmetry of the same magnitude is the rotation of the polarization direction of a feed. An $\approx 1^\circ$ rotation results in a signal of 3 mK in D band (Table 6). It cannot be ruled out that some part of the asymmetry is due to this, though it would be coincidental to have the asymmetry so similar in both feeds. In the HEMT channels, the signature of the asymmetry due to feed rotation is opposite in the two polarizations. As the chopper sweeps, the emission for one polarization goes up while that from the other polarization goes down. There is no evidence for such a signal.

The offsets for Ka and Q band are similar to those shown in Figure 6 and in Figure 1 of Herbig et al. (1998). Before accounting for the chopper emission, the magnitude is between 4 and 8 mK. The offsets in Ka and Q bands in the SK experiment were 0.5–2 mK, considerably smaller than those observed here. This is attributed to the fact that the TOCO/QMAP system is, by necessity, much more compact: the chopper is closer to the feed horns and the ground screens are closer to the main beam.

After accounting for the polarized chopper emission and the alignment of the chopper, both of which can be computed accurately, there is still a residual polarized offset in all channels of magnitude 2–8 mK. In particular, the observed residual offset is always largest in the horizontal polarization as shown for D band in the bottom panels of Figure 6. The offsets are largest in Q band, and thus no particular characteristic spectrum is identified. This suggests that the source is modulated cavity emission, thermal emission from the enclosure, or a combination of both. We have not been able to definitively identify the mechanism responsible for the effect, though the most likely source is the shallow angle diffraction of the chopper cavity emission into the parabola. Other potential sources either are too small or do not have the correct polarization.

The offsets discussed in this section are not atypical for CMB experiments. They correspond to the raw detector

output before any of the symmetries or modulations of the experimental design have been utilized. In §§ 11 and 12 the offsets *after* the strong spatiotemporal filter of the experimental method has been applied are discussed.

6. ELECTRONICS AND DATA ACQUISITION

Because it was balloon borne, QMAP was by necessity self-contained. It had its own command telemetry and CCD-based pointing system (Devlin et al. 1998) though it used the National Scientific Balloon Facility (NSBF) transmitters to relay data. To operate remotely in Chile as the TOCO experiment, a transmitter was added to telemeter a compressed version of the data from the telescope on Cerro Toco to the ground station in San Pedro de Atacama, 35 km away. A block diagram of the telescope electronics, data system, and telemetry is shown in Figure 7.

6.1. *Electronics*

The eight radiometry signals are processed in the backpack. Each signal is square law detected with detector diodes, amplified, and sent with differential line drivers to a processing board. On the processing board, the signal is high-pass filtered with a two-pole RC network with $f_{3\,\mathrm{dB}} = 1$ Hz to remove the DC level that is separately recorded. This filter introduces a small but stable electronic offset. The high-passed analog signal is then digitized using an 18 bit $\Sigma\Delta$ analog-to-digital converter (ADC).[22] The serial digital signal is sent through a shift register and latch that converts it to a 32 bit parallel word accessible by a computer. The use of $\Sigma\Delta$ ADCs is advantageous over sampling ADCs because of their superior differential nonlinearity specification, which is important when signals comparable to or smaller than the 1 bit level are of interest. Additionally, these ADCs incorporate a digital antialiasing filter, eliminating any temperature dependence or drift in this component of the electronic bandpass.

In the CMB analysis, HEMT data from 14 to 55 Hz ($4 < l < 200$) and SIS data from 15 to 60 Hz ($4 < l < 500$) are used. The electronic bandpasses are defined on the lower end by the high-pass filter and on the high end by the $\Sigma\Delta$ chip. Over our frequency range, the phase response of the chip is linear with frequency, so the $\Sigma\Delta$ introduces a time delay in the signal. The amplitude response over the CMB frequencies varies by less than 0.4% over this range.

6.2. *Computers and Telemetry*

Two single-board computers, which handle the data and the pointing, are located on the telescope. They are synchronized with a common clock and communicate remotely with the computers operating at the base station. In the following, the focus is on the configuration for TOCO.

The "Data PC" logs the detector output and the position of the chopping mirror as well as various voltages, currents, temperatures, etc., which monitor the telescope. Two versions of the data are recorded. A complete version (≈1 Gbyte day^{-1}), which is used in the final analysis, is stored on a 4 Gbyte hard drive in the data computer. This drive is contained in a pressurized vessel to prevent damage resulting from operation at high altitude.[23] These drives are swapped

[22] This constitutes one-half of an Analog Devices AD1878.

[23] When not enclosed in a pressurized and dust-free container, most hard drives, especially high-capacity ones, were found to fail on a timescale of a day.

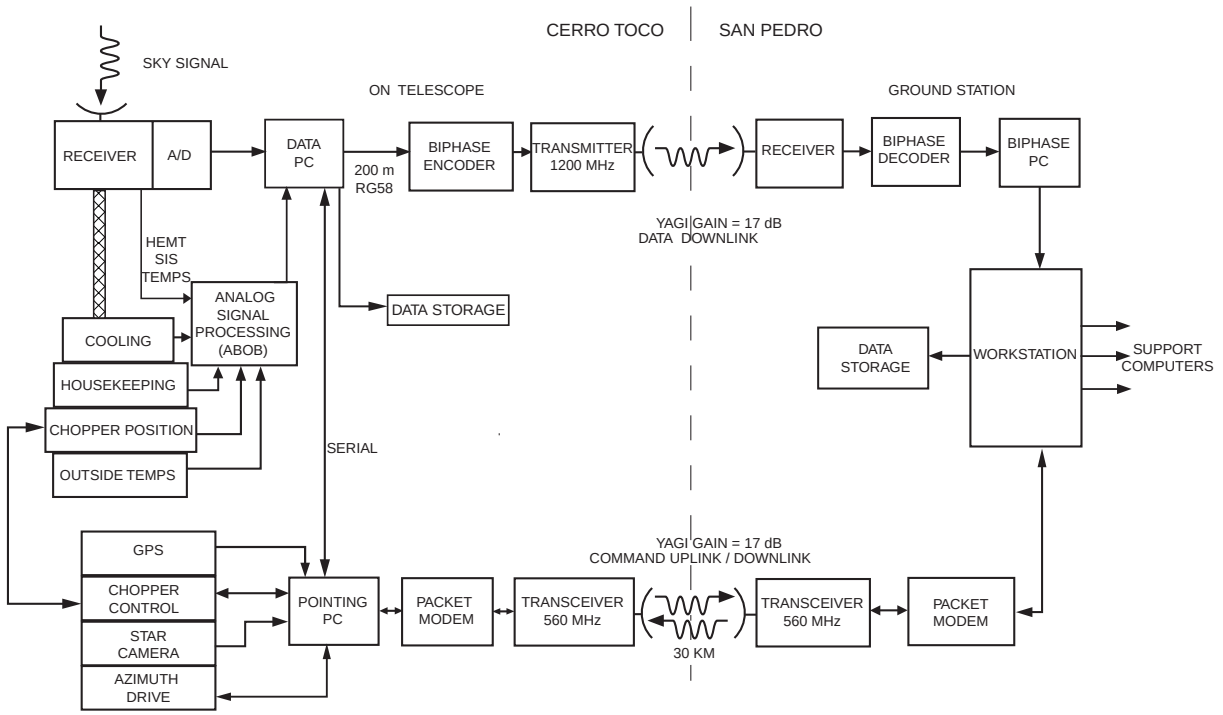

FIG. 7.—Layout of electronics and telemetry system for TOCO. The components on the left are on Cerro Toco, and those on the right are at the ground station in San Pedro (a hotel room in La Casa de Don Tomás), at a comfortable living altitude. The up/down command link is a 40 W Motorola GM300 radio communicating via a Paccomm packet modem.

TABLE 7
TELESCOPE AND CHOPPER MOTION

Parameter	QMAP96a	QMAP96b	TOCO97	TOCO98
Chopper frequency, f_c (Hz)	4.7	4.6	4.6	3.7
Chopper amplitude in azimuth, ϕ_c(max) (deg)	±10	±2.5	±2.96	±2.02
Elevation at center of chop, θ_{el} (deg)	40.7	40.1	40.5	40.63
Azimuth of center of chop,[a] θ_{az} (deg)	Scanned	Scanned	204.9	207.47
Amplitude of wobble (s)	100	50	None	None
Amplitude of wobble in azimuth (deg)	±5	±1.5	None	None

[a] This is the physical motion in a horizontal plane. The amplitude on the sky is $2\phi_c \cos\theta_{el}$.

out every 2–4 days. The data are then uploaded onto the computer system in the ground station and stored on exabyte tapes. A second compressed version of the radiometry and housekeeping data is biphase encoded and sent real time to the ground station.

The "Pointing PC" records the position of the 17 bit absolute digital encoder on the telescope azimuthal bearing, controls and monitors the azimuthal drive motor, records the time from a Global Positioning System (GPS) receiver, and interprets commands sent remotely from the ground station. A CCD camera and Matrox digital image processing board can track stars during calibration and pointing verification procedures. The command status and all other information on the pointing PC are passed to the data PC for logging. The Pointing PC can also reboot the Data PC, an operation sometimes found necessary.

Two radio links allow us to communicate with the telescope from the ground station. A high-frequency link at 1.4 GHz (bandwidth of 100 kHz) with a 2 W transmitter links the data computer with a ground station PC providing the biphase data. A marine radio operating at 460.5 MHz communicates via a packet modem with the pointing computer, providing commanding.

The ground station computers receive and store the data, archive the data to tape, and run the commanding, display, and alarm software. From the ground station, the telescope can be slewed in azimuth, chopper parameters can be adjusted, and the cooling power (to stabilize the temperature of the warm electronics) can be increased or decreased. Most major systems can be turned on and off remotely.

7. OBSERVATIONS

While both QMAP and TOCO were designed to measure the anisotropy, their approaches were completely different. QMAP was designed to make a true map. In the first flight of QMAP, the chopper swept horizontally at 4.7 Hz (see Table 8) and the gondola wobbled in azimuth with a period of 100 s about a meridian containing the north celestial pole. This gondola motion, combined with the rotation of the Earth, produced a highly interlocking scan pattern that allowed for the clean separation of instrumental effects from the celestial signal (de Oliveira–Costa et al. 1998a).

The TOCO scan was designed to measure the angular power spectrum.[24] The telescope optical axis is fixed in azimuth and elevation, as indicated in Table 7, and the chopper sweeps the beam across the sky with the parameters shown in Table 8. The beams cover an annulus around the south celestial pole as shown in Figure 8.

The TOCO observing site is located at an altitude of 5200 m on Cerro Toco in the northern Atacama desert in Chile near the borders of Argentina and Bolivia. The latitude is 22°.95 south, and the longitude is 67°.775 west. A building for an abandoned sulphur mine blocks the occasional 60 knot winds. The Atacama is one of the highest, driest deserts in the world and is therefore a good place for millimeter- and centimeter-wave observations. The weather is good enough for D-band CMB observations ≈50% of calendar time between September and January.

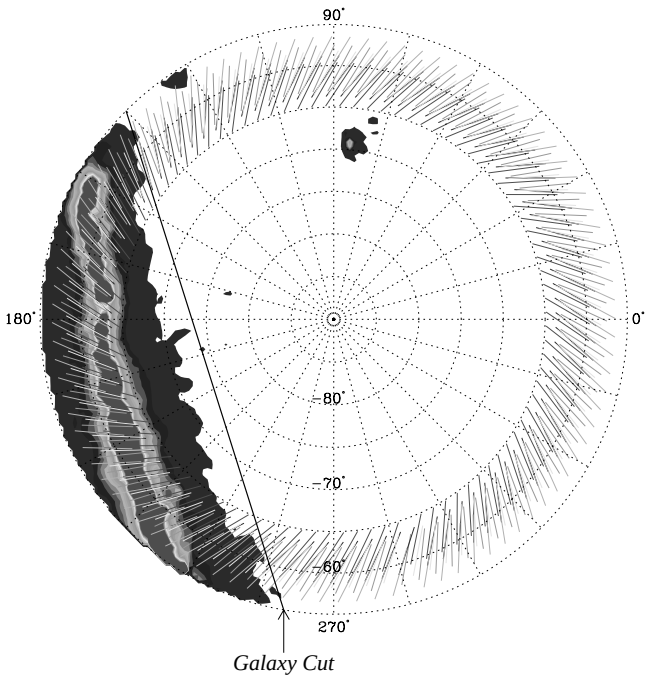

FIG. 8.—Scan pattern for the TOCO98 campaign around the south celestial pole. The scans are shown as straight lines for each feed for 15 minute intervals around the sky. A more detailed picture would show the lines with slight curvature to account for the projection. The center of the chop is at an azimuth of 207°.5 and an elevation of 40°.6. The chopper sweeps out 6°.12 on the sky as it scans in azimuth. This results in a ring around the south celestial pole approximately centered on $\delta = -61°$. The map of the galaxy is from Schlegel et al. (1998). [*See the electronic edition of the Journal for a color version of this figure*.]

[24] We decided against observing on both sides of the south celestial pole (which would have produced interlocking scans, thereby facilitating map production) to maximize the stability of the instrument and to minimize the complexities of the analysis.

TABLE 8
OBSERVING PARAMETERS

Campaign	Ka1	Ka2	Q1	Q2	Q3	Q4	D1	D2
QMAP96a								
$\Theta_{\rm FWHM}$ per scan[a]	20	20	30	30	30	30	...	...
Samples per $\Theta_{\rm FWHM}$ (F/S)[b]	0.78/3.2	.78/3.2	0.56/2.7	0.56/2.7	0.58/2.7	0.58/2.7	...	...
Point-source sensitivity $\Gamma(\nu_c)$ (μK Jy^{-1})	128	128	132	132	129	129	...	...
QMAP96b								
$\Theta_{\rm FWHM}$ per scan	5	5	8	8	8	8	...	...
Samples per $\Theta_{\rm FWHM}$ (F/S)	3.1/6.5	3.1/6.5	2.4/5.7	2.4/5.7	2.3/5.6	2.3/5.6	...	...
Point-source sensitivity $\Gamma(\nu_c)$ (μK Jy^{-1})	136	136	146	146	120	120	...	...
TOCO97								
Samples per chop, N_s	80	80	80	80	80	80	320	...
$\Theta_{\rm FWHM}$ per scan	6	6	9	9	9	9	30	...
Samples per $\Theta_{\rm FWHM}$ (F/S)[b]	1.3/3.0	1.3/3.0	1.0/2.6	1.0/2.6	1.0/2.6	1.0/2.6	1.1/5.2	1.7/6.7
Point-source sensitivity $\Gamma(\nu_c)$ (μK Jy^{-1})	131	131	128	120	119	118	87.3	49.5
TOCO98								
Samples per chop, N_s	80	80	80	80	80	80	320	320
$\Theta_{\rm FWHM}$ per scan	4	4	6	6	6	6	20	20
Samples per $\Theta_{\rm FWHM}$ (F/S)	1.9/3.6	1.9/3.6	1.5/3.2	1.5/3.2	1.4/3.0	1.4/3.0	1.7/6.7	2.5/8.1
Primary aperture efficiency, η_p	0.58	0.58	0.65	0.62	0.56	0.55	0.52	0.24
Chopper aperture efficiency, η_p	0.10	0.10	0.11	0.11	0.10	0.10	0.087	0.040
Point-source sensitivity $\Gamma(\nu_c)$ (μK Jy^{-1})	121	121	138	131	119	116	117	54.7

[a] The number of beam FWHM contained in one scan.
[b] F/S refer to the fast and slow parts of the sinusoidal motion near the center and edges of the chop. The sample frequencies for Ka and Q bands were 752, 736, 368, and 296 Hz for QMAP96a through TOCO98. For TOCO97, the D sample frequency was 1472 Hz, and for TOCO98 it was 1184 Hz. The sky is not Nyquist sampled at the center of the chop. This is accounted for in the mapmaking and beam synthesis. The e^{-1} point of the beams, $l_e = (16 \ln 2)^{1/2}/\theta_{\rm FWHM}$, is $l_e = 212$, 273, and 955 for Ka, Q, and D, respectively. The QMAP96a undersampling limits the map reconstruction in the current pipeline to $l \approx 180$.

8. CALIBRATION

Calibration is the largest source of experimental uncertainty for both QMAP and TOCO as it is for many other CMB experiments. In general, calibration is dominated by systematic effects. Multiple independent measurements are required to determine the uncertainty. Short of this, one's knowledge of the experiment is called upon to set the uncertainty and its distribution.[25]

A calibration for TOCO involves the following steps: (1) position the telescope so that Jupiter either rises or sets through the azimuthally swept beam; (2) make a map of the source and find the best-fit amplitude, position, and beam profile; (3) compute the brightness of Jupiter, accounting for its position with respect to the Earth; and (4) correct for slow drifts in calibration, correct for the electronic response of the receivers, and convert Rayleigh-Jeans to thermodynamic temperature. A similar procedure was used for QMAP. In the following, each element of the calibration and its associated uncertainty is considered.

There are two general classes of calibrators: those that fill the beam and point sources. FIRS (Ganga et al. 1994), BOOMERanG, and MAXIMA used the dipole as calibrated by both FIRAS and DMR aboard *COBE*. The dipole signal corresponds to angular scales larger than, and detection frequencies lower than, those used for CMB data analysis. Thus, knowledge of the electronic transfer function, beam profile, and spatial filtering is necessary for the extrapolation. At the other extreme, point sources are at smaller angular scales and higher postdetection frequencies than those used for CMB analyses. They have the advantage that the calibration and beam profile are measured simultaneously. Still, though, one must account for the electronic transfer function and spatial filtering.

QMAP was calibrated with Cas A,[26] and TOCO was calibrated using Jupiter. As the beam sweeps across the source, the detector output is given by

$$\mathscr{C}V(t) = \frac{1}{2}\int_\nu \int_\Omega \int_{t'} A_e(\nu) g(\nu) S_\nu(\mathbf{\Omega}) \times P_n[\nu, \boldsymbol{x} - \boldsymbol{x}'(t')] I(t - t') d\boldsymbol{x}\, d\nu\, dt' \ , \quad (8)$$

where V is the voltage out of the detector, A_e is the effective area of the telescope dish, $g(\nu)$ is the passband of the receiver, S_ν is the source surface brightness in units of W m^{-2} sr^{-1} Hz^{-1}, P_n is the normalized gain of the antenna, $\boldsymbol{x}$ is

[25] One may, for example, conservatively use the difference between two measurements as the uncertainty (e.g., de Bernardis et al. 2000) even though the formal uncertainty is the difference divided by $\sqrt{2}$. To determine error bars on quantities derived from the data, one marginalizes over the distribution that describes the calibration. Generally, the distribution is taken as Gaussian, though one might reach different conclusions if a different distribution in fact described the data.

[26] Cas A is also known as 3C 461 ($l = 111.^\circ7$, $b = -2.^\circ1$).

TABLE 9
SUMMARY OF CONTRIBUTIONS TO CALIBRATION UNCERTAINTY FOR INDIVIDUAL CHANNELS

Channel	σ_S (%)	σ_Ω (%)	σ_V (%)	$\sigma_{\rm drift}$ (%)	σ_η (%)	σ_I (%)	σ_C (%)
D1	5	5.5	3	4	1	1	9.1
D2	5	5	3	4	1	1	8.8
TOCO HEMTs	5	5	3	4	...	1	8.7
QMAP HEMTs	2.7	5	3	...	...	5	8.1

NOTE.—The intrinsic Jupiter calibration uncertainty is given by σ_S (§ 8.1), σ_Ω is the uncertainty in measured solid angle (§ 8.2), σ_V is the uncertainty in measured Jupiter brightness temperature (§ 8.2), $\sigma_{\rm drift}$ (§ 8.3) is the uncertainty due to the calibration drift between observations, σ_η refers to the Rayleigh-Jeans–to–thermodynamic conversion due to the uncertainty in the centroid, and σ_I is the uncertainty on the electronic bandpass correction. These calibration errors are for temperature.

the direction on the sky, and I is the impulse response function of the electronics.[27] Here $\mathscr{C}$ is the calibration constant that relates the source temperature to the measured voltage. Sampling is not explicitly accounted for in the integral.

Each term in equation (8) has an error associated with it that contributes to the net uncertainty. The effects include (1) σ_S, the intrinsic uncertainty in the brightness temperature of the source at the calibration frequency extrapolated from previous measurements; (2) σ_V, the uncertainty in the measured temperature of the source; (3) σ_Ω, the uncertainty in the measured solid angle of the beam, which includes any beam smearing; (4) the uncertainty in the measured receiver bandpass, σ_g, and center frequency, σ_ν; (5) $\sigma_{\rm drift}$, the uncertainty in the change of the calibration between when it is measured and when it is applied; and (6) σ_I, the uncertainty in the frequency response of the instrument. Items (2) and (3) are derived from measurements of the source and are covariant; generally one conservatively treats them as independent uncertainties. Combining these sources, the intrinsic calibration is given by

$$\left(\frac{\sigma_C}{C}\right)^2=\left(\frac{\sigma_S}{S}\right)^2+\left(\frac{\sigma_V}{V}\right)^2+\left(\frac{\sigma_\Omega}{\Omega}\right)^2+\left(\frac{\sigma_{\rm drift}}{\rm drift}\right)^2+\left(\frac{\sigma_I}{I}\right)^2 . \quad (9)$$

These terms are evaluated in the following and summarized in Table 9.

8.1. *Calibration Source Brightness Temperatures*

The flux from a source is typically given as $f_\nu = \int S_\nu(\theta,\phi)d\Omega$ Jy (1 Jy $= 10^{-26}$ W m^{-2} Hz^{-1}) as a function of frequency. A power-law model is used to extrapolate the calibration frequencies to the observation frequency, $f_\nu = f_0(\nu/\nu_0)^\beta$. When the source angular size is a significant fraction of the beam or is changing in time, as it is for planets, it is more convenient to use the brightness temperature.

8.1.1. *Cas A Flux for QMAP*

Cas A is unresolved at the QMAP beam size, and the correction for its finite size is negligible. From a combination of the data (Baars et al. 1977; Chini et al. 1984; Mezger et al. 1986), $\log(S_\nu/{\rm Jy}) = (5.713 \pm 0.023) - (0.759 \pm 0.006)$ $\log(\nu/{\rm MHz})$ at epoch 1980 (Herbig et al. 1998). At 31.3 GHz, the mean frequency of the QMAP Ka bands, the flux corresponds to 199.9 Jy. Baars et al. (1977) give the percentage annual decrease as $\delta S_\nu/S_\nu = 0.97(\pm0.04) - 0.3$ $(\pm0.04)\log(\nu/{\rm GHz})$, hence this value is reduced to 183 Jy for epoch 1997. When one takes into account all of the above uncertainties, including σ_ν, the uncertainty is $\sigma_S/S = 8.7\%$ for both Ka and Q bands.

After the QMAP data release, Mason et al. (1999) reported $S_{\rm Cas,1998} = 194 \pm 4.7$ Jy at 32 GHz, 195 Jy for epoch 1997. This measurement, which is very close to our frequency, greatly reduces the uncertainty associated with the interpolation and secular decrease. When the uncertainty in the central frequency is included (Table 1), the uncertainty is $\sigma_S/S = 2.7\%$. For Q band, the flux is 159 ± 4.8 Jy. The slightly larger uncertainty is from the extrapolation from 32 to 41 GHz. The result is an increase in the temperature scale of the QMAP data by 6.6% and reduction in the calibration uncertainty, σ_S.

8.1.2. *Jupiter Temperature for TOCO*

The brightness temperature of Jupiter is measured by Ulich (1981), Griffin et al. (1986), Goldin et al. (1997), and Mason et al. (1999) and is taken to be 152, 160, and 170 K in Ka, Q, and D band, respectively, with an intrinsic calibration uncertainty of $\sigma_S/S = 5\%$. As the temperature is a weak function of frequency across our bands, the uncertainties resulting from σ_ν and σ_F are negligible. The Jupiter calibration temperature is obtained by scaling the brightness temperature by the ratio of the solid angle of Jupiter (determined from ephemerides) to the measured solid angle of the beam. A typical measured temperature of Jupiter is 15, 30, and 350 mK in Ka through D1 bands, respectively.

Finally, one applies a correction to convert small changes in antenna temperature to small changes in thermodynamic CMB temperature:

$$\eta = \left(\frac{\partial T_{\rm ant}}{\partial T_{\rm CMB}}\right) = \frac{x^2 e^x}{(e^x-1)^2} , \quad (10)$$

where $x = h\nu/kT_{\rm CMB}$. For the TOCO98 D-band data, the data are multiplied by η^{-1}, or 1.66 for D1 and D2, to convert from data calibrated on Jupiter's brightness temperature to thermodynamic units referenced to the CMB. The Ka- and Q-band data are multiplied by 1.02 and 1.05, respectively. The uncertainty in these measurements depends on the

[27] A typical frequency-dependent loss in the system has a negligible affect on the calibration.

knowledge of the band centroids and introduces $\leq 1\%$ uncertainty.

8.2. *Measured Beam Solid Angle and Temperature*

To convert the measured fluxes to a temperature, the beam solid angle must be known. Table 5 gives the beam determination for all campaigns along with the results of a computer model. For QMAP, the solid angle was determined from one in-flight mapping of Cas A (Herbig et al. 1998). The statistical uncertainty on the fit varied between 1% and 3% depending on the flight and band. As the beam fitting includes modeling of the instrumental offsets, there is additional systematic error resulting in a net uncertainty of $\sigma_\Omega/\Omega = 5\%$. For TOCO, the beam solid angles were determined from a global fit to over 70 Jupiter calibrations made during good weather. This was done separately for both campaigns. All results from the four campaigns are consistent with our models. From all of the beam measurements, we conclude that the uncertainty on the solid angle is 5% for Ka and Q bands, 5% for D1, and 5.5% for D2. These values are dominated by systematic errors.

It is often convenient to parameterize the beams with a two-dimensional Gaussian profile. For Ka and Q bands, this introduces a negligible error. In the TOCO97 (Torbet et al. 1999) analysis, the measured Ka and Q beam profiles were used in place of the parameterized profiles, and there was less than 1% difference in the final results. The D-band channels are less well approximated by Gaussian profiles, and thus one must use the measured profile for accurate results as done in Miller et al. (1999).

For each calibration, a seven-parameter model of the position of the source, the best two-dimensional Gaussian parameterization including orientation, the amplitude, and an offset is fitted to the data. For QMAP, the 1%–2% statistical error on the amplitude is dominated by a 3% systematic uncertainty in the algorithm to extract the amplitude. In the TOCO experiment, the standard deviation of the fitted amplitude is 4%–10% for all the HEMT channels in both seasons. The variance is a result of atmospheric fluctuations and finite HEMT sensitivity and thus averages down as the square root of ≈ 20 independent high-quality maps in each season to a value of 2%. There is a small additional uncertainty due to the fact that not all fitting algorithms give the same results. The net result is to increase the uncertainty in the amplitude to $\sigma_V/V = 3\%$.

8.3. *Calibration Drift*

The physical temperature of the TOCO instrument can vary by 50 K in a day. Even though all critical components are thermally regulated, there are temperature changes that lead to changes in gain. Jupiter was observed, on average, within 2 hr of beginning the CMB observations. Changes in system gain on timescales shorter than 24 hr were monitored with an internal calibration signal ("cal pulse") with an effective temperature of ≈ 1 K in all bands. This pulse was turned on 40 ms twice every 200 s. The amplitude of the pulse was regressed with the body temperatures of the noise sources, warm electronics temperatures, and cryogenic temperatures in all bands. The fit coefficients are consistent with laboratory measurements and show that the pulse amplitude is constant but that the system gain is a function of the microwave amplifier temperatures.

For TOCO, a typical long-term (50 days) variation is 15% in Ka band, 5% in Q band, and 20% in D band. The cal pulse amplitudes follow the general trends in the Jupiter calibrations in all bands. From the cal pulses and the Jupiter observations, a calibration drift model is derived that is applied to the data. In D band, atmospheric fluctuations made use of the cal pulses to correct drifts over periods of less than 6 hr problematic. The uncertainty in the model is estimated to be 5%. A similar approach was taken with QMAP though the cal pulses were clearer, so the uncertainty in correcting for the 5% drift is negligible.

8.4. *Electronic Passband*

Observing a point source is similar to exciting the electronics with a pulse. Consequently, there are frequency components up to $f \approx 4(\phi_c \cos\theta_{\rm el}\theta_{\rm FWHM})f_c$ (Table 7) of the postdetection electronics. The CMB signal is at comparatively lower frequencies. From a model of the electronic response of the system, including sampling, one finds that the CMB data should be reduced by 1.7% in D band, 1.5% in Q band, and 1% in Ka band for TOCO and 1.5% for QMAP over what one would get without the correction. The uncertainty in this is 1% for TOCO and 5% for QMAP. These shifts were not reported in the original papers as they were much smaller than the uncertainty.

There is a slight undersampling during the fastest part of the chop as shown in Table 7. To check for a possible systematic effect in TOCO associated with this, calibrations were done with the source at the center of the chop and off to one side and with different chopper amplitudes. The results of these tests are statistically consistent with the nominal calibrations. For TOCO, the CMB anisotropy results are insensitive to the slight undersampling because the CMB detection frequency is far below the sample frequency (as a result of the beam synthesis) and because in the beam synthesis the sky scan is simulated.

In the first flight of QMAP the undersampling was not included in detail in the mapmaking. Thus, the QMAP data should only be considered valid up to $l \approx 180$.[28] For both flights, the calibration data were processed in a manner similar to the mapmaking, so beam smearing effects were accounted for in an average sense.

The phase response of the full instrument as a function of frequency was measured in the laboratory and determined from observations of the Galaxy and Jupiter. The phase is linear over the range of frequencies applicable to both CMB and point-source observations.

8.5. *Combining the Calibrations between Bands and Systematic Shifts from Previous Results*

Both QMAP and TOCO have multiple detectors, the measurements of which are combined into one angular spectrum. The net calibration uncertainty is a combination of terms that are completely correlated between channels, such as σ_S, σ_Ω, $\sigma_{\rm drift}$, and σ_I, and terms that are uncorrelated, such as σ_V and σ_η. When the data are combined, the last two terms become negligible. The uncertainties are 8% for D1+D2, for the TOCO HEMTs, and for the combination

[28] Neither the undersampling nor the calibration shift was accounted for in Xu, Tegmark, & de Oliveira–Costa (2002) though the effects are small.

of the D1+D2+HEMTs. For QMAP the net uncertainty is 7.6%. In the regions where the QMAP and TOCO angular spectra overlap, only σ_S and σ_Ω are correlated and the combined uncertainty is 6.4%.

These uncertainties are slightly different from those previously quoted for these experiments and are the result of a complete reassessment of the calibration errors. To correct the previously published results for calibration, the QMAP data should be multiplied by 1.051, the TOCO D-band data (Miller et al. 1999) should be multiplied by 0.983, and the TOCO HEMT data (Torbet et al. 1999) should be multiplied by 0.99.

9. OBSERVING THE ANISOTROPY

The anisotropy is a two-dimensional random field in temperature. The goal of CMB anisotropy experiments is to measure the characteristics of that field. The three methods in use are direct mapping, time domain beam synthesis, and interferometry. For a small number of detectors, direct mapping is the most efficient, beam synthesis is the next most efficient, and interferometry is the least efficient, as discussed in § 10. The best strategy to use, though, depends as much on the control of potential systematic errors as on raw sensitivity.

The QMAP experiment was designed to make a direct map. By this we mean that the time-ordered data are assigned a sky pixel number as they come out of the detector. Slow drifts in the detector output may be removed from the map using a variety of methods (Cottingham 1987; de Oliveira–Costa et al. 1998a; Hivon et al. 2002). For all methods, though, a heavily interlocking scan strategy is required for robust results. QMAP produced multiple $\approx 0.^{\circ}8$ resolution maps of the CMB from two flights. These maps were found to be consistent with each other and with the SK maps (Xu et al. 2000). In other words, two entirely separate experiments measured the same temperature variations in the sky in overlapping regions. The other mapping experiments to do this are *COBE*/DMR (Smoot et al. 1992) with FIRS (Ganga et al. 1994) and *COBE*/FIRAS with *COBE*/DMR (Fixsen et al. 1997). A wide range of systematic checks have been applied to QMAP, and it passes them all.

The TOCO experiment used time domain beam synthesis.[29] To our knowledge, the method was first employed in Netterfield et al. (1995). Since the SK experiment, we have refined the technique, applied it to a multifeed system, and incorporated numerous cross-checks and systematic checks of the robustness of the solution. Most of the remainder of this paper is devoted to describing those checks.

10. TIME DOMAIN BEAM SYNTHESIS

As with all ground-based CMB experiments, the effects of atmospheric fluctuations must be strongly suppressed. TOCO uses the chopping flat to scan the beam across the sky in a sinusoidal pattern (§ 4.2). In a postdetection analysis, the time-ordered data are multiplied by synthesis vectors, $\mathrm{SV}_{n,i}$, that have half the period of the chopper cycle. Thus, the data with the chopper moving in one direction are co-added with the data with the chopper moving in the other direction to form

$$t_n = \sum_{i=1}^{N_c} \mathrm{SV}_{n,i} d_i \ , \tag{11}$$

where d_i is the vector containing the raw data from a full chop cycle, n is the index or "harmonic" of the synthesized beam, and N_c is the number of samples in a chop cycle.

There is no set prescription for $\mathrm{SV}_{n,i}$. The best choice depends on the scan pattern (e.g., sinusoidal or triangular), the desired degree of orthogonality between synthesized beams, the shape of the resulting window function, and the orthogonality to any potential offset. For instance, one may pick $\mathrm{SV}_{n,i}$ so that t_n is insensitive to the secant dependence of the atmospheric gradient. For the sinusoidal scan patterns, a useful set is given by

$$\mathrm{SV}_{n,i} \propto \cos\left(\phi_n + \frac{\pi(n-1)\{1-\sin[2\pi(i-1/2)/N]\}}{2}\right) ,$$
$$i = 1, \ldots, N_c \ , \tag{12}$$

though ultimately the $\mathrm{SV}_{n,i}$ are tuned. The synthesis vectors are effectively apodized sine functions, each of which is designed to produce a different effective antenna pattern and thus probe a different angular scale.

The phase of the electronic signal with respect to the position of the beam on the sky, ϕ_n, is determined by forming the quadrature signal (data from the first half of chopper sweep minus data from the second half resulting in minimal sensitivity to celestial signals) as a function of phase for each harmonic. Then the phase that nulls the galactic signal over 25 of the best observing days is found. There is a small harmonic-dependent component to the best-fit phase that is well modeled with a linear fit. The phase shift is incorporated into equation (12) for all analyses. The galaxy-null determined phases agree with the phases determined from Jupiter observations, derived with completely independent code. In addition, the entire data analysis is redone after setting the phase ahead and behind the best fit by twice the error derived in the fit. There are no changes in the final results from this.

The resulting effective antenna sensitivity patterns, or synthesized beams $H(\boldsymbol{x})$, are given by

$$H(\mathbf{x}) = \left\langle \sum_i \mathrm{SV}_i G(\boldsymbol{x} - \boldsymbol{X}_i) \right\rangle_{\text{R.A. bin}} , \tag{13}$$

where the center of the main beam is located on the sky at position $\boldsymbol{X}_i$, SV_i is the synthesis vector, and

$$G(x,y) = \frac{1}{2\pi\sigma_x\sigma_y} \exp\left(-\frac{x^2}{2\sigma_x^2} - \frac{y^2}{2\sigma_y^2}\right) \tag{14}$$

is the main beam pattern of the telescope pointed at the center of the chop. Here x measures the position in the azimuthal direction, y changes with elevation, and the beamwidth of the telescope is $\sigma = \theta_{\mathrm{FWHM}}/(8\ln 2)^{1/2}$. Beam smearing due to the finite size of the sky bins is incorporated into equation (13). As tests, the analog-to-digital sampling and the change in the effective horizontal beamwidth as a function of chopper speed are included in equation (14). These effects are negligible. The synthesized beams are then nor-

[29] Atmospheric fluctuations preclude direct mapping from the ground.

malized, by adjusting the amplitude of $SV_{n,i}$, so that

$$\int |H(\boldsymbol{x})| d\boldsymbol{x} = 2 \, . \tag{15}$$

In summary, the synthesis vectors and beam synthesis incorporate all known aspects of the motion of the beam on the sky.

Data are binned according to right ascension at the center of the chopper sweep into 768 "base bins" around the complete circle shown in Figure 8. The base bins are subgrouped into $N_{\rm R.A.}$ right ascension bins, where $N_{\rm R.A.}$ depends on the harmonic. Thus, the average in equation (13) depends on harmonic. To avoid statistical bias, it is important that the mean, sample variance, and error on the mean in each of the $N_{\rm R.A.}$ bins are computed for *all* the data that land in a bin in a given night. For example, for the 1998 4-pt,[30] Q-band beam, there are $N_{\rm R.A.} = 20$ bins around the circle, so in one night $\approx 1.7 \times 10^4$ values of t_4 (eq. [11]) are averaged together for each bin. At low l, the variance in any R.A. bin is larger than that expected from detector noise alone due to atmospheric fluctuations. For integrations longer than roughly 3 minutes, the noise is stationary for the cuts described below. Finally, the results from individual nights are averaged.

The harmonics are analyzed individually at low l or in groups at higher l. Data from different detectors are also combined. The full theory covariance matrix, C_T, is computed for each harmonic or combination (Bond 1996) along with the Knox filter (Knox 1999) and effective spherical harmonic index, l_e, of the observations. The noise covariance matrix, C_N, is computed from the data. Other than detector noise, which is uncorrelated between bands, the dominant contribution is the atmosphere. Unlike SK, the frequency bands are not subdivided and there is no east-west chopping.

For each group of harmonics, the likelihood as a function of the band power, δT_l^2, is found according to[31]

$$L(\delta T_l^2) = \frac{1.}{2\pi^{N/2} |\boldsymbol{M}|^{1/2}} \exp\left(\frac{-t^T \boldsymbol{M}^{-1} t}{2}\right) , \tag{16}$$

where $\boldsymbol{M} = C_T(\delta T_l^2) + C_N$. All the analysis is done as a function of δT_l^2, though δT_l is reported because it gives a direct measure of signal-to-noise ratio (S/N) as the detector output is proportional to temperature.

It is sometimes convenient to estimate the S/N for a single measurement for a single harmonic. This can then be generalized to a set of N independent measurements (Knox 1995). The measured rms amplitude of the sky fluctuations is given by $\Delta = \delta T_l [I(W)]^{1/2}$, where $I(W) = \sum_l (W_l/l)$, with W_l the window function, encodes the efficacy of the synthesized beam (Bond 1995). The noise of any measurement is given by $\kappa_n \tilde{\boldsymbol{T}}/\tau_{\rm obs}^{1/2}$, where[32] $\kappa_n = \left(N_c \sum_{i=1}^{N_c} {\rm SV}_{n,i}^2\right)^{1/2}$, $\tau_{\rm obs}$ is the time spent observing a point, and $\tilde{\boldsymbol{T}}$ is given by equation (2). From fits to the computed $I(W)$, it is found that $[I(W)]^{1/2} \approx 2.6/n^{0.75} \approx 6/\sigma_b^{0.25} l_e^{0.75}$, where n denotes the n-pt function, σ_b is the Gaussian width of the beam, and l_e is the associated effective spherical harmonic index. The S/N for a particular measurement is then

$$\begin{aligned} {\rm S/N} &= \frac{\delta T_l \sqrt{I(W)} \tau_{\rm obs}^{1/2}}{\kappa_n \tilde{\boldsymbol{T}}} \\ &\approx \frac{0.7}{\sigma_b^{0.5} l_e^{0.8}} \frac{\delta T_l \tau_{\rm obs}^{1/2}}{\tilde{\boldsymbol{T}}} \approx \gamma^{\rm TDBS} \frac{\delta T_l \tau_{\rm obs}^{1/2}}{\tilde{\boldsymbol{T}}} \, . \end{aligned} \tag{17}$$

This result may be interpreted as saying that for a fixed sensitivity, $\tilde{\boldsymbol{T}}$, and a flat angular spectrum, δT_l, beam synthesis reduces the effective temperature of the sky by $\gamma^{\rm TDBS} = 0.7/\sigma_b^{0.5} l_e^{0.8}$. This form fits Ka-band through D-band data to 30% accuracy for TOCO.[33]

It is worth contrasting beam synthesis in interferometry with time domain beam synthesis. In interferometry, each baseline yields one synthesized beam enveloped by the primary beam pattern of a single element. A similar expression to equation (17) obtains for interferometers with Gaussian main beams of width $\sigma_b^{\rm Int}$ (Hobson, Lasenby, & Jones 1995; White et al. 1999):

$${\rm S/N} = \frac{\sqrt{2}}{\sigma_b^{\rm Int} l_0} \frac{\delta T_l \tau_{\rm obs}^{1/2}}{\tilde{\boldsymbol{T}}} = \gamma^{\rm Int} \frac{\delta T_l \tau_{\rm obs}^{1/2}}{\tilde{\boldsymbol{T}}} \, , \tag{18}$$

where $l_0 = 2\pi u_0$ is determined by the separation of the two antennae. For the 5-pt Q-band synthesized beam, $\theta_{\rm FWHM} = 0.^\circ 7$ ($\sigma_b = 0.0052$) and $l_e = 87$. Similar coverage in l-space would be obtained with an interferometer with $\theta_{\rm FWHM} = 4.^\circ 86$ ($\sigma_b^{\rm Int} = 0.036$) and $l_0 = 87$. From these, $\gamma^{\rm TDBS} = 0.27$ and $\gamma^{\rm Int} = 0.45$. To the level of accuracy of the fitting functions, these are equivalent.

The sensitivity advantage of time domain beam synthesis is that multiple n-pt functions are measured simultaneously with a single detector. In the parlance of Fourier transform spectroscopy, there is a multiplex or "Felgate" advantage over an interferometer with just a few antennae. However, because the number of interferometer baselines scales as $n_a(n_a - 1)/2$, where n_a is the number of antennae, large interferometers achieve high sensitivity (Padin et al. 2001; Pryke et al. 2002). For the ideal mapping experiment, with minimal baseline subtraction, the advantage over both interferometry and time domain beam synthesis is that in a fixed amount of time more spatial modes can be measured.

11. DATA SELECTION

Most of the analysis effort goes into data selection and testing to make sure that the selection does not bias the final result. The largest cuts remove data contaminated by the galaxy, by the atmosphere, and by unstable offsets. Partial descriptions of the cuts are given by Miller et al. (1999) and Torbet et al. (1999). In this section we describe the cuts for the TOCO98 D-band data and the consistency checks as they are indicative of the process for all channels. A summary of the cuts is given in Table 10.

11.1. *Cuts to the Time Line*

The initial cuts are made to the raw time-ordered data in order to excise extreme events, such as a nearby object enter-

[30] Following the notation in Netterfield et al. (1997), we call a synthesized beam with n lobes an n-pt beam (see Fig. 5).

[31] In this paper, the band power is reported following Bond as opposed to Netterfield. The difference is $2(l+1)/(2l+1) \approx 0.2\%$ at $l = 200$.

[32] For the classic single difference, $\kappa = \{2[1^2 + (-1)^2]\}^{1/2} = 2$.

[33] Other functional forms work as well. This is presented to aid in estimating the S/N. For SK, which used different criteria to synthesize the beams, $\gamma^{\rm TDBS} = 3.6/\sigma_b^{0.5} l_e$, roughly a factor of 2 higher at low l. However, the window functions were less well localized.

TABLE 10
CUTS FOR TOCO98 D-BAND DATA

Parameter	Value
Data Cuts for the Season	
Total number of nights analyzed[a]	54
Number of nights used (D1)[b]	28 (52)
Number of nights used (D2)[b]	23 (47)
Percentage of data kept in a "good" 24 hr period (%)	53
Net percentage kept[c] (%)	26
Data Cuts for a Typical Good Night	
Galaxy (%)	32
rms (overlaps with Galaxy cut) (%)	24
Chopper (%)	3
Pointing (%)	1
GPS (overlaps with rms and Galaxy cut) (%)	5
Net cut before beam synthesis (%)	41
Net cut after beam synthesis (%)	45
Net cut to the binned data[d] (%)	47

[a] This is the number of consecutive nights on which the SIS system operated. After 54 days, the refrigerator cold head malfunctioned and heated to the point where the SISs were unusable.
[b] Numbers in parentheses are in %.
[c] This is the net observing efficiency for data of sufficient quality for CMB analysis.
[d] This corresponds to 53% of data kept in a "good" 24 hr section.

ing the beam or very bad weather. Data are examined in 6.5 s averages (24 chop averages with $f_c = 3.7$ Hz). The internal calibration pulses are removed and a rough cut is made at a nominal rms level based on the long-term observing characteristics. This cut removes ≈50% of the data.

The next set of rms cuts is made to the synthesized data. In general, the higher harmonics are less sensitive to atmosphere and therefore require less severe cuts. The data are binned into 15 minute averages and, for each harmonic on each day, the minimum value of the average rms is selected as the baseline. For D1, all data within 25% of the minimum are accepted for harmonics 8–21. For harmonics 5–7 everything within 20% is accepted. For the case of D2, harmonics 8–17 are cut at 30%, and 5–7 are cut at 20%. Harmonics ≤ 4 are rejected entirely as they are corrupted by atmospheric fluctuations.

We analyze 28 nights for D1 and 23 nights for D2. (The number is higher for D1 because of high offsets in D2 on several nights leading to the decision to exclude these data from the analysis.) In order to prevent signal contamination from times of large atmospheric fluctuations, the previous and subsequent 15 minute segments are eliminated from each segment cut by the above criteria. The effect of this cut is to keep 5–10 hr blocks of continuous good data in any day and to eliminate transitions into periods of poor atmospheric stability. On a typical day that passes the initial rms cut, an additional 40% of the synthesized data are removed as a result of atmospheric fluctuations. The net result is that 26% of the data are kept.

As discussed above, data are placed into 768 base bins in right ascension with R.A. = 0° corresponding to the first bin. All data falling between bins 288 and 555 are cut in order to eliminate observations of the Galaxy from the CMB analysis. This is equivalent to cutting all data with 135° < R.A. < 260° centered at $\delta = -60°$. By observing at an azimuth of 208°, the Galactic cut occurs during daylight, when the 144 GHz data are not generally useful for CMB observations because of the atmosphere. The Galactic cut overlaps well with the atmospheric cut. In a 24 hr day in which there are minimal atmospheric fluctuations, only 35% of the data are cut.

When the rms chopper position over a single chop deviates by more than 0°.015 from the average position, the data are cut. This includes times when the chopper is intentionally shut off as a result of testing and maintenance as well as time during high winds. This cut eliminates ≈3% of the data.

The absolute timing is done through GPS. Data are eliminated during GPS dropouts. There was also an error in the first frame of each logical file that made the GPS read out incorrectly for that frame. The first file in each set is therefore rejected (≈5% of the data). The files were generally started directly following a calibration or during the day, thus the percentage of these data that would otherwise be retained for CMB analysis is small.

11.2. *Cuts to the Binned Data*

The goal of the cuts to the binned data is to ensure that only long periods of uninterrupted data are included in the final analysis. The low-density regions are cut by removing any base bin with fewer than 15 of the adjacent bins filled. This is done twice to ensure that stragglers are removed. Finally, the entire file (approximately 1 day) is removed if there are fewer than 100 usable bins (approximately 3 hr of uninterrupted clean data). More than 90% of the nights analyzed for CMB anisotropy have continuous 5–10 hr blocks of data.

11.3. *Offset Removal*

An offset is the value of a given harmonic when the signal on the sky is zero. Equation (11) gives the expression for an element of synthesized data. Each element in the final data file is the average value over the R.A. bin,

$$t_n^{\rm bin} = \frac{1}{N_{\rm cib}} \sum_{j=1}^{N_{\rm cib}} t_{n,j} \ , \tag{19}$$

where $t_{n,j}$ is the result from each chop cycle and $N_{\rm cib}$ is the number of chopper cycles in an R.A. bin. Thus, on a given night, each R.A. bin has a single value of $t^{\rm bin}$ for each harmonic. These values are examined as a function of R.A. bin, and both a slope and a mean are removed from each harmonic on each night before the nights are combined. The slope subtraction has little effect on the final result; its removal is prudent though not essential.

Because the best data do not exactly overlap each night, a potential bias occurs when the mean and slope are subtracted over different regions of sky. Typical offsets for the TOCO98 D-band data are ≈150 ± 75 μK in absolute value and drift over a timescale of days. When each full night of data of one harmonic is co-added and analyzed as a function of night throughout the campaign, χ^2/ν for deviation from a flat line is between 1 and 4. The high-l offsets are generally more stable. Because only large sections of contiguous data are kept and the offset is stable, the effect of slightly different sky coverage per evening is negligible. In the analysis, the slope and offset removal is approximated as removing a

single mean and slope from the entire data set as discussed below.

The chopper position–dependent offsets (Fig. 6) discussed in § 5 are effectively filtered by the beam synthesis. This is checked by applying the synthesis vectors to the average chopper-synchronous signal by setting $d_i = O_i$ in equation (11). The variation in the resulting synthesized offset is then examined as a function of harmonic and observing night. The standard deviation of the resulting O_n is less than 20 μK for the harmonics used in the analysis. Because the offsets are subtracted, this variation does not affect the final result.

11.4. *Ergodicity of Noise*

Well-defined noise properties are essential for the analysis of CMB data. After the offset subtraction and data cuts, the t_n for each harmonic are binned as pixel number versus night of observation. The average error bar on t_n is independent of night and pixel number. In addition, for a given pixel, the variation in the mean value from night to night is consistent with the average of the variances separately determined each night.

In the high-S/N channels, δT_l^2 can be found by forming

$$\delta T_l^2 = \frac{\Delta_{\rm tot}^2 - \Delta_{\rm inst}^2}{I(W)} \ , \qquad (20)$$

where $\Delta_{\rm tot}^2$ is the total variance of the data for one harmonic and $\Delta_{\rm inst}^2$ is the average variance due to instrument noise. For $l \leq 200$, the results from this calculation are within 10% of the results for the full likelihood analysis (Torbet et al. 1999). At $l < 150$ the noise is potentially the most problematic because the offsets are generally larger and the contribution from the atmosphere is larger than for the higher l data. That a simple method based on average noise properties gives the same answer (within 1 σ) as the full likelihood analysis, with its detailed attention to correlations and drift subtraction, gives us confidence that the noise estimates are robust and stable. There is nothing in the instrument or sky of which we are aware that changes at the temporal frequencies and spatial scales associated with $l > 200$. Although the S/N is lower for large n-pt beams, the data are stable and insensitive to cuts.

12. LIKELIHOOD ANALYSIS AND TESTS OF DATA SELECTION

The most likely value of δT^2 as a function of angular scale is found with a Bayesian likelihood analysis of the cleaned data. The method follows the analysis of the SK data though the correlation matrices are considerably simpler as a result of the observing strategy and the focal plane array. One feature of the likelihood analysis is that channels and harmonics can be combined in a precise and unambiguous way to increase the S/N. An added benefit of the combined bands is that correlation between combined bands is reduced over that for a single harmonic. The likelihoods for the HEMT data and SIS data are shown in Figure 9.

Tests are made to ensure that data selection eliminates the atmospheric and instrumental contaminants without biasing the result. This is done by performing a set of internal consistency tests or null tests. Data are multiplied by several different sets of synthesis vectors that have no sensitivity to the sky signal, and the analysis is carried out in the same way as for the data that have been multiplied by the sky-sensitive synthesis vectors. The data have been properly selected when the set of null tests fails to show a signal for individual synthesized beams. The data selection is therefore blind to the signal on the sky, minimizing potential bias introduced by expectations.

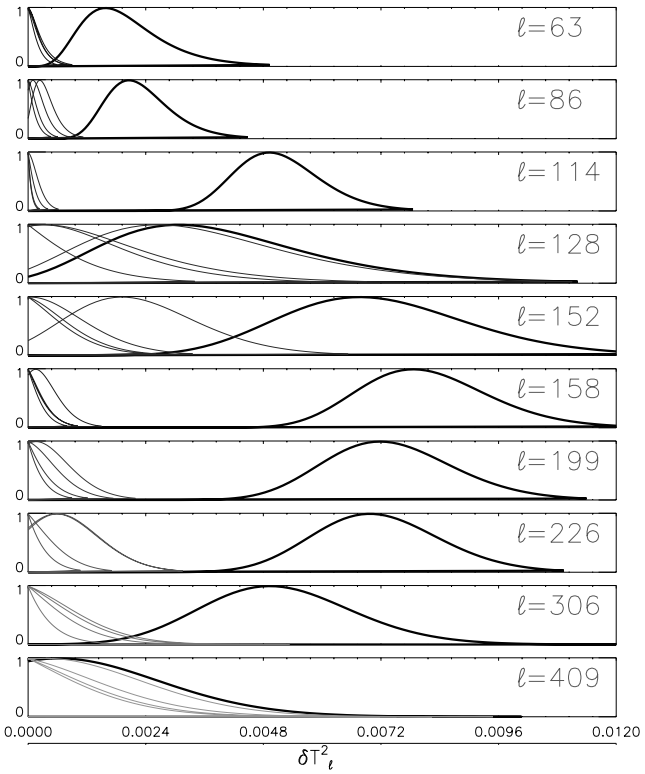

FIG. 9.—Likelihood plots for the TOCO data. All likelihoods are normalized to unity at the maximum. The x-axis is δT_l^2 in units of (mK)^2. The value on the right of each panel corresponds to the effective l for each Knox filter. The thick contours are for the data. The thinner lines are the likelihoods for the null tests: quadrature, fast dither, slow dither, and first half minus second half signals. The $l = 128$ D-band channel is possibly contaminated by the atmosphere, though the distribution of the null tests is consistent with noise. The null test that is close to the signal is from the slow dither and of all the null tests is the one most different from zero. Such $\approx$1.5 σ deviations are not statistically unexpected. This figure clearly shows the rise and fall of a peak in the CMB angular spectrum. Furthermore, it shows that the null tests are consistent with zero signal. The D-band data are at $l = 128$, 152, 226, 306, and 409. [*See the electronic edition of the Journal for a color version of this figure.*]

The four null tests probe different timescales. The quadrature signal is sensitive to variations at 2 Hz. For the fast and slow dither, the difference between subsequent 0.5 and 10 s averages, respectively, is examined. We also examine the difference night to night and between the first and second half of the campaign. In the TOCO98 analysis of individual harmonics for each channel, there was one "failure" (>2 σ deviation from a null signal) out of 120 tests, well within expectations. The results of some of the null tests for the full bands are shown in Figure 9.

12.1. *Effects of Selection Criteria on the Data*

Following the selection of the best cuts, the selection criteria or methods are changed in four ways. For each test, the full likelihood analysis is performed. The nominal cut, though, is based on the null tests, not the data. When the

selection criteria are changed, the null tests either show signs of contamination, when the likelihoods change, or are unaffected, when the likelihoods do not change. In the following the D-band data are the focus, though similar tests were performed on the HEMT data.

Test 1.—The minimum number of filled bins on a given day is increased from 100 (≈3 hr) to 250 (≈8 hr), and all days not common to both D1 and D2 are rejected from the analysis. The result is a decrease in the significance of the detections (due to permitting less data in the final analysis) but a change of less than 1 σ for the two low-l points and less than $\sigma/2$ for the three high-l points.

Test 2.—The nominal calibration model is determined from fits to Jupiter and the internal calibration pulses. Instead, this analysis simply uses the calibration value of the closest Jupiter calibration. The result is a change of less than $\sigma/2$, primarily as a result of a different calibration.

Test 3.—The harmonic-dependent cut to the synthesized data is made more stringent. Instead of cutting 45% for a typical good 24 hr day as shown in Table 10, 65% is cut. The more stringent cut is most pronounced in the lower harmonics because they are most affected by atmospheric contamination. The cut results in upper limits for the $l = 128$ and 152 points, consistent with the decreased amount of data. Above the 7-pt, the amount of data cut and the resulting likelihoods change very little. This test is also done by eliminating just 50% (as opposed to 45%) with similar results.

Test 4.—The initial cut is applied only to the raw data, so on a typical good day 41% of the data are kept (before the Galactic cut). This has the effect of introducing some atmospheric contamination. The result is that the $l = 128$ and 152 points show an increase in signal of 0.8 and 1.3 σ, respectively, while the data points corresponding to the highest three groups of harmonics show no significant change.

The TOCO98 D-band data have been emphasized because the points at $l = 128$ and 152 are more sensitive to the cuts than all the other data. This is due to the large atmospheric opacity at 144 GHz and large angular scales. The nominal cut corresponds to the best null tests and corresponds roughly to the sections of raw data one would select by eye. The D-band data for $l > 200$ are insensitive to the cuts as are all of the HEMT data.

12.2. *Correlations*

The off-diagonal terms in the noise correlation matrix, C_N, are small. The atmospheric correlation coefficients between channels (Q and Ka band) for TOCO97 and between D1 and D2 for TOCO98 are of order 0.05. The autocorrelation function of the data is examined for individual harmonics and finds negligible correlations between R.A. bins (as a result of atmospheric fluctuations). The largest off-diagonal terms in $\boldsymbol{M}$ are less than 0.4 and are in C_T. The likelihood is stable to changes of ≈30% the values of the off-diagonal terms.

13. TESTS FOR SYSTEMATIC EFFECTS

There are potential sources of systematic error that would not be revealed by the tests described above. These sources of error, along with their maximum contribution to the data, are summarized in Table 11 and described below. Again, the D-band data are the focus. No effect significantly affects the final results, and in particular no effect can produce the decrease in power that is observed between $l \approx 200$ and 400.

TABLE 11

POST–BEAM SYNTHESIS SYSTEMATIC EFFECTS

Systematic Effect	Maximum Resultant Change in $\delta T/T$ (%)
Chopper jitter	0.1
Chopper zero-offset drift	0.2
Miscalibration of chopper amplitude	3
Miscalibration of azimuth	0.1
Miscalibration of elevation	1
Incorrect determination of beam size	1
Electronic roll-off (between data points)	0.2
Gain variation in offsets	3
Chopper phase offset	0.5

The systematic effects involve either beam smearing (§§ 13.1–13.5) or another mechanism (§§ 13.6–13.9). For those effects related to beam smearing, the uncertainties are found through computing $I(W)$ for the smeared beam. The fractional error for an individual harmonic is given by

$$\frac{\Delta(\delta T_l)}{\delta T_l} = \frac{1}{\delta T_l}\frac{\partial(\delta T_l)}{\partial\sqrt{I(W)}} = \frac{\delta\sqrt{I(W)}}{\sqrt{I(W)}} \, . \qquad (21)$$

The actual fractional uncertainty in groups of harmonics will be smaller because the uncertainties are computed for the highest harmonic in a band group, which is the one with the fewest number of physical beams between nulls in the synthesized beam and therefore the one most affected by beam smearing.

Uncertainties are computed for D1, unless otherwise noted, because it has a smaller beam than D2 and is consequently more affected by smearing. Nominal values of $[I(W)]^{1/2}$ are the following: $[I(W)]^{1/2} = 0.377$ for D1 and $[I(W)]^{1/2} = 0.350$ for D2 for the case of the 16-pt and 17-pt beams, respectively.

13.1. *Chopper Jitter*

Jitter in the chopper position, due to wind or electronic malfunction, smears the beam. All data for which the rms of the chopper position deviates more than 0°.015 from the nominal position are rejected from the analysis. The maximum resulting uncertainty in either D1 or D2 in any harmonic (resulting from an increase in beam size in the direction parallel to the chop of 0°.015) is $\delta[I(W)]^{1/2} = -3.0 \times 10^{-4}$, or $\delta T_l/T_l \approx 0.1\%$.

13.2. *Chopper Zero-Offset Stability*

Beam smearing can be caused by a drift in the electronic zero point of the chopping mirror. The zero point is monitored throughout the campaign. From the beginning to the end of the analyzed data, the zero point drifts by ≈0°.03. An upper limit on the extent to which this can affect our result is found by considering a smearing of the beam in the direction parallel to the chop of 0°.03. This results in $\delta[I(W)]^{1/2} = -7 \times 10^{-4}$, or $\delta T_l/T_l \approx 0.2\%$.

13.3. *Miscalibration of Azimuth*

If the azimuth changed over a period of time, the true beam could be uncertain by an amount equivalent to this change. The relative uncertainty in azimuth is less than 0°.01, which could manifest itself as an increase in beam size in the direction parallel to the chop by a maximum of 0°.01. The resultant uncertainties are $\delta[I(W)]^{1/2} = -2.0 \times 10^{-4}$, or $\delta T_l/T_l < 0.1\%$.

13.4. *Miscalibration of Elevation*

Similarly, if the elevation changed over time, the true beam could be uncertain by an amount equivalent to this error. The relative error in elevation is less than 0°.01, which could manifest itself as an increase in beam size in the direction perpendicular to the chop by a maximum of 0°.01. The resultant errors are $\delta[I(W)]^{1/2} = -3 \times 10^{-3}$, or $\delta T_l/T_l \approx 0.8\%$.

13.5. *Incorrect Determination of the Beam*

If the beam was incorrectly measured, there would be an effective beam smearing in either the direction parallel or perpendicular to the chop. Errors in the $\theta_{\rm FWHM}$ of the beam are ≈0°.005 and ≈0°.008 for D1 and D2, respectively. The maximum resulting error in either channel in any harmonic is $\delta[I(W)]^{1/2} = 2.5 \times 10^{-3}$, or $\delta T_l/T_l \approx 0.7\%$. This is an upper limit because errors in the determination of the beam affect the calibration as well and are therefore partially compensated.

13.6. *Miscalibration of Chopper Amplitude*

If the chopper amplitude were miscalibrated, the assumed number of physical beams fitting into a given synthesized beam could be wrong. The amplitude of the chopper is known to less than 2% uncertainty (2 σ). If the value used in the analysis were wrong by this amount, the resulting change would be $\delta T_l/T_l < 3\%$ for the worst-case harmonic. Most harmonics show a change of $\delta T_l/T_l < 1\%$. The entire spectrum also shifts a small amount in l. For a 2% increase in the chopper amplitude, there is an ≈2% shift in each point to lower l values. The sign of this effect is reversed if the chopper amplitude is smaller than the assumed value.

13.7. *Electronic Roll-Off*

The likelihood contours shown in Figure 9 correspond to different postdetection frequencies as well as different l. The point at $l = 226$ contains data from the 6-pt to 7-pt beams in D1 and the 6-pt to 9-pt beams in D2 corresponding to $f \approx 25$ Hz. The point at $l = 409$ contains the 12-pt to 16-pt beams in D1 and 12-pt to 17-pt beams in D2, corresponding to $f \approx 50$ Hz. As shown by calculation and measurement, the electronic transfer function changes by less than 0.2% over this range and thus does not affect the results.

13.8. *Gain Variation in the Offsets*

Variations in the cryogenic temperatures and the temperature of the warm electronics box lead to variations in the gain. If the effects of the decrease in gain of the warm amplifiers, the decrease in sensitivity of the SIS mixers, and the increase in output of the calibration source with increasing temperature are combined during the period of CMB observations, there could be an undetected gain drift of ≈1%. In addition, there could be other gain effects of order 3% that would escape detection because the variation in atmospheric opacity would mask their signature in the cal pulse. Because of the large heat capacity, such variations would occur on the timescale of hours.

Changes in gain affect the offset. Since the offsets are different for different synthesized beams, it is possible to affect the spectrum through a gain change. When the average offsets for the combined harmonics are multiplied by a gain variation of ≈3%, a signal with amplitude ≈3 μK at low harmonics and less than 2 μK at higher harmonics results. Not only is this signal small, but it is largely accounted for through the offset and slope subtraction.

13.9. *Chopper Phase Offset*

If the phase of the chopper were to drift, the sky signal would be smeared because the beam would not be positioned according to the nominal chopper template. The cut on the chopper amplitude rms corresponds to a phase shift of 0.5 samples. A shift of this size contributes less than 0.5 μK in δT_l.

14. FOREGROUND EMISSION AND RESULTS

After the raw data have been reduced and binned on the sky, the foreground emission contribution from our Galaxy and from other galaxies is determined. The foreground contribution at these frequencies, Galactic coordinates, and angular scales is not large (Tegmark et al. 2000; Coble et al. 1999; Masi et al. 2001). This is clear from Figure 10. The amplitude of the first peak is measured to be roughly the same from 30 to 144 GHz when the flux is expressed as changes in a 2.725 K thermal emitter. The spectral index of the fluctuations is $\beta_{\rm CMB} = \ln(\delta T_{144}/\delta T_{36.5})/\ln(144/36.5) = -0.04 \pm 0.25$, where δT_{144} is the weighted mean of the two highest points for the D-band data and $\delta T_{36.5}$ is a similar quantity for the HEMT data (36.5 GHz is the average HEMT frequency). For the CMB, $\beta_{\rm CMB} = 0$. For dust, $\beta_{\rm RJ} = 1.7$ corresponds to $\beta_{\rm CMB} = 2.05$; for free-free emission, $\beta_{\rm RJ} = -2.1$ corresponds to $\beta_{\rm CMB} = -1.75$.

Fits to foreground templates were not done for Torbet et al. (1999) and Miller et al. (1999), and there was the possibility that the amplitude of the peak had a contribution from foreground emission (Page 1999; Knox & Page 2000). However, the mean frequency spectrum of the peak clearly singles out the CMB as the dominant source of the fluctuations. In addition, the angular spectrum of foreground emission is much different than the measured angular spectrum of the CMB.

To quantify the foreground emission, a fit is made to four templates: the SFD dust map ($T_{\rm SFD}$) (Schlegel, Finkbeiner, & Davis 1998), the Haslam synchrotron map ($T_{\rm H}$) (Haslam et al. 1982), and the radio ($T_{r\text{-pt}}$) and *IRAS* ($T_{\rm IR\text{-}pt}$) source compilations from the WOMBAT compilation (WOMBAT 2001).[34] A fit has not been made to the Hα maps that trace microwave free-free emission. However, fits to SK (Gaustad, McCullough, & Van Buren 1996; Simonetti, Dennison, & Topansa 1996) found that the free-free contribution was negligible. In addition, cross-correlations between the WHAM Hα maps (Haffner, Reynolds, & Tufte

[34] http://astron.berkeley.edu/wombat.

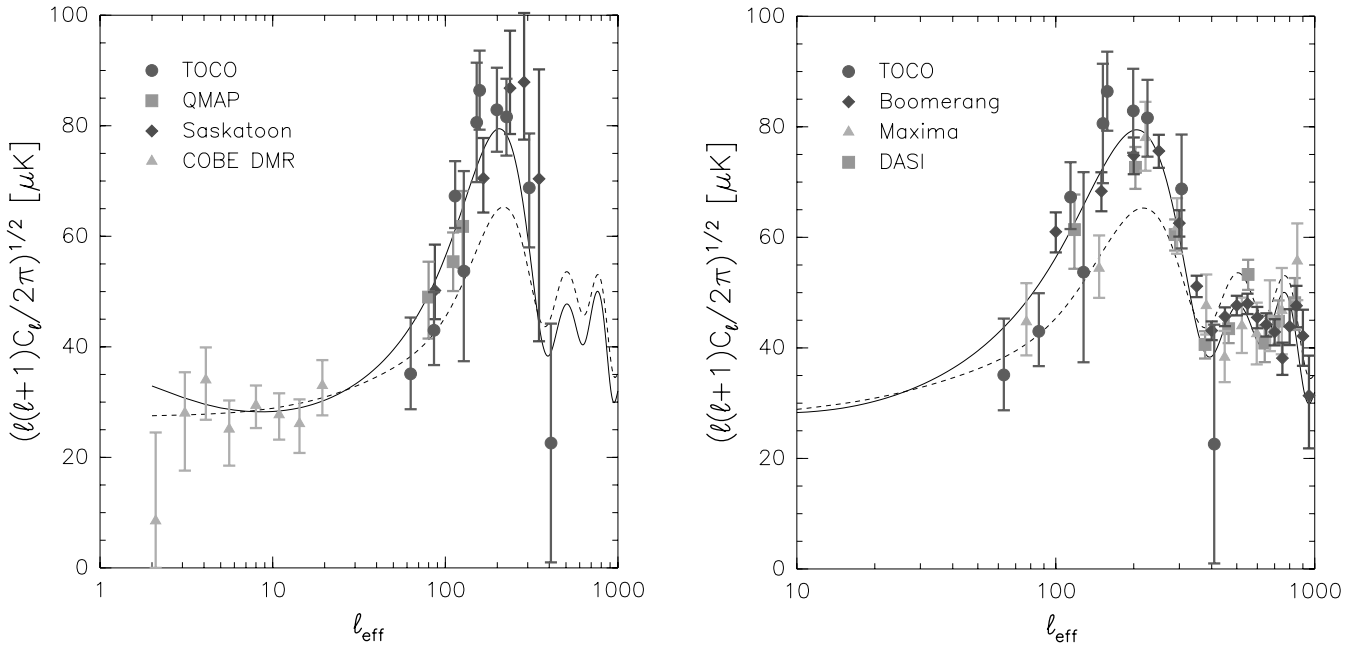

FIG. 10.—Combination of the SK, QMAP, and TOCO data with all corrections. Following Netterfield et al. (1997), we plot the position of the maximum of the likelihood with error bars that encompass 68.3% of the likelihood for all points where there is a significant detection. For the last TOCO point we plot a representation of 1 σ based on Bond et al. (2000). The plot is made with δT as opposed to δT^2 because δT directly shows the S/N. For example, $\delta T = 5 \pm 1$ μK has S/N = 5, whereas the equivalent $\delta T = 25 \pm 10$ μK has an apparent S/N ≈ 3. The models are "standard CDM" (*right*) and the best fit from Jaffe et al. (2001) (*left*). Calibration uncertainty is not included. [*See the electronic edition of the Journal for a color version of this figure*.]

1999) and other CMB maps, including QMAP, do not show a significant contribution (de Oliveira–Costa et al. 2002).

There is a correlation between CMB maps at frequencies less than 90 GHz and dust maps (Kogut et al. 1996; de Oliveira–Costa et al. 1997; Leitch et al. 1997). The mechanism responsible for the correlation is not yet certain (de Oliveira–Costa et al. 2002) though spinning dust grains are a strong candidate (Jones 1997; Drain & Lazarian 1998). The dust-correlated foreground component is larger than the free-free component traced by Hα between 20 and 40 GHz and is not correlated to the Haslam map (de Oliveira–Costa et al. 1998b). Thus, the SFD map is a good tracer of foreground emission for the HEMT data. The Galactic latitude of the CMB scan covers between $b = -8°$, $l = 280°$ and $b = -34°$, $l = 335°$ as shown in Figure 8. Our sky scan passes near the Large Magellanic Cloud (LMC, $b = -32.^\circ9$, $l = 280.^\circ5$), and data are removed from near it. During the day, known sources in the Galactic plane (Puchalla et al. 2002) are observed.

The template fitting procedure is restricted to the section of sky analyzed for CMB anisotropy. The goal is to assess the contribution to the CMB results rather than to characterize foreground emission. First, the template map is multiplied by the synthesized beam in a manner such that the full CMB observing strategy is reproduced. Except in the case of the Haslam map for the $l > 200$ D-band data (where no correlation is expected), the size of the synthesized beam lobes is larger than the resolution of the template map. Next, for each harmonic, the template is fitted with

$$\chi^2 = \sum_{k=1}^{N_{n,\rm bins}} \left[t_k - (a_0 T_{r\text{-pt}} + a_1 T_{\rm IR\text{-}pt} + a_2 T_{\rm H} + a_3 T_{\rm SFD})\right]^2 w_k \ , \quad (22)$$

where $N_{n,\rm bins}$ is the number of filled bins around the sky for the n-pt function ($<N_{\rm R.A.}>$), t_k is the CMB temperature (eq. [19]), and w_k is the statistical weight of each measurement. The fits are performed as a function of angular scale and frequency. Where the fit result is significant, as shown in Table 12, the foreground component is subtracted in quadrature from δT_l as determined from the likelihood analysis.[35]

The fit results may be summarized as follows: (1) The dominant source of contamination at 30 and 40 GHz is from the radio point sources as traced by the 4.85 GHz PMN catalog (Griffith & Wright 1993; Condon, Griffith, & Wright 1993; Wright et al. 1994) on which the WOMBAT maps are based. The extrapolation to 30 GHz is known to be problematic because the source spectra vary from source to source (Puchalla et al. 2002). We cannot rule out a contribution from sources that are not traced by the extrapolated PMN survey, but because of the measured spectrum of the peak, such a contribution cannot be too large. Over our sky coverage $\approx$600 deg^2, $\approx$100 sources are accounted for. Most of the contribution comes from the largest 10% and is spread throughout the observing region. (2) Contributions from synchrotron emission are negligible unless the synchrotron spectral index varies so much that the Haslam map is not a good template. The largest rms of the Haslam map, after applying the beam synthesis, is 0.6 K. When extrapolated to 30 GHz with a spectral index of $\beta_{\rm RJ} = -2.7$, one gets 5.5 μK, consistent with the fitted values. The fitted dust contribution at the 30 GHz $l = 60$ and 40 GHz $l = 80$

[35] This simple treatment, in which chance alignments of the CMB with the foreground are ignored (e.g., de Oliveira–Costa et al. 1997) and the foreground is subtracted in quadrature, is sufficient because the foreground contribution to the CMB is less than 4% in all cases. Future work will address the full treatment and the Galactic plane.

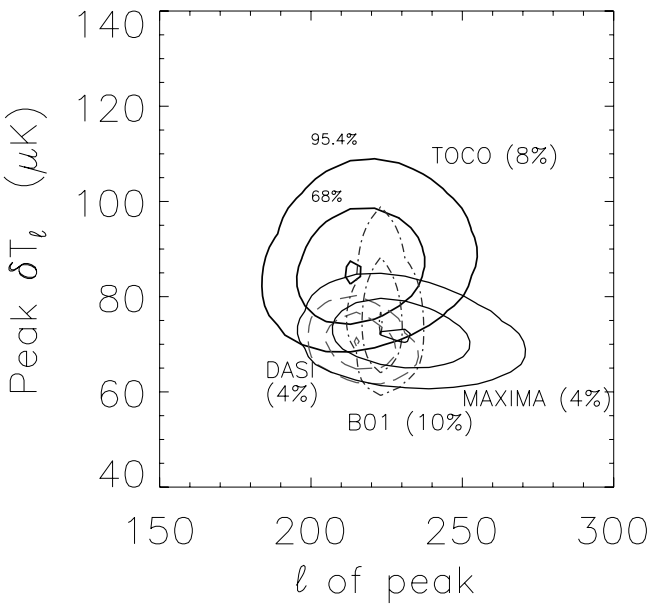

FIG. 11.—Position and amplitude of the first peak following the Gaussian temperature method (Knox & Page 2000). For TOCO $l_{\rm peak} = 216 \pm 14$ and $\delta T_l = 86 \pm 9$ μK. These values are slightly different than those reported before ($l_{\rm peak} = 212$ and $\delta T_l = 88$ μK) because of the calibration and foreground corrections. The BOOMERanG data set (Netterfield et al. 2002) gives $l_{\rm peak} = 224$ and $\delta T_l = 75$ μK. (The North American flight is omitted.) The BOOMERanG beam uncertainty is not accounted for; it will tend to broaden the distribution in l. MAXIMA (Lee et al. 2001) yields $l_{\rm peak} = 230$ and $\delta T_l = 72$ μK, and DASI (Halverson et al. 2002) gives $l_{\rm peak} = 216$ and $\delta T_l = 71$ μK. These values are close (<1 σ) to the values found in de Bernardis et al. (2002) using different methods. Calibration uncertainty has been taken into account though the correlations between bands have not. When treated consistently, TOCO, B01, MAXIMA, and DASI pick out values for the peak position and amplitude that are within 2 σ of each other. However, the exact results have some dependence on the peak finding methodology. For all experiments the curves are normalized at $l = 10$ to DMR; this is most important for DASI and less important for the other experiments. [*See the electronic edition of the Journal for a color version of this figure*.]

points is small but consistent with the picture of 30 GHz dust-correlated emission. (3) There is no significant contamination at 144 GHz from either dust or point sources.

Table 13 gives the results from TOCO along with the revised results from QMAP and SK[36] based on foreground analyses and new information on the calibration. The final results for all three experiments are shown in Figure 10 along with a comparison to recent experiments.

[36] In addition to some authors on this paper, SK was analyzed by Ed Wollack and Norm Jarosik.

15. DISCUSSION

Since the discovery of the anisotropy (Smoot et al. 1992), there have been many CMB anisotropy experiments at $l < 1000$ in addition to the ones noted thus far (ARGO, de Bernardis et al. 1994; Ratra et al. 1999a; MSAM, Wilson et al. 2000; UCSB/SP, Gundersen et al. 1995; White Dish, Ratra et al. 1998; Python, Ruhl et al. 1995; BAM, Tucker et al. 1997; IAB, Piccirillo & Calisse 1993; Tenerife, Hancock et al. 1994; MAX, Lim et al. 1996). The SK experiment was the first to show the rise of the CMB angular spectrum in the region between $l = 50$ and 250 independent of any other experiment, for example, *COBE*/DMR. At the time, the amplitude of the peak was considered high, although it is consistent with the subsequently popular ΛCDM models and more precise measurements.

Though a straightforward read of the data previous to TOCO suggested a peak at $l \approx 200$ (e.g., SK and OVRO, Leitch et al. 2000; SK and CAT, Baker et al. 1999), there were lingering questions of cross calibration and point-source subtraction. In fact, if one did not include the SK data, the combined analysis of UCSB/SP, ARGO, MAX, White Dish, and SuZIE favored an open universe (Ratra et al. 1999b). Dodelson & Knox (2000) showed that TOCO alone singled out a flat universe as the best model. Others (Bahcall et al. 1999; Bond, Jaffe, & Knox 2000), including Dodelson & Knox (2000), showed that the combination of all the data singled out a flat universe.

QMAP was designed to measure the anisotropy by direct mapping. Degree resolution high-S/N maps were made that could be compared to each other and, because they covered the same region of sky, confirmed the $l < 150$ SK results (Xu et al. 2000). The strategy of direct total power mapping was later employed by the BOOMERanG and MAXIMA experiments, which ushered in much higher S/N subdegree resolution mapping.

The TOCO experiment showed both the rise and fall of the first peak and showed that its spectrum was that of the CMB with a single instrument (Fig. 10). These results have since been amply verified by BOOMERanG, MAXIMA, and DASI. The rise to the maximum has high S/N; the fall for $l > 200$ is also clearly evident though worth quantifying. Miller et al. (1999) reported that the 95% upper limit of the last point in D band was just below the 2 σ lower bound of the point of the peak. The second to last point was not included in the assessment. Here a more complete analysis is performed. We focus on just the last three D-band points, δT_{226}, δT_{306}, and δT_{409}, because the calibration uncertainty is common to all and drops out of the analysis. There are two ways

TABLE 12
SUMMARY OF FOREGROUND CONTRIBUTIONS

Foreground	$l = 60$[a]	$l = 85$	$l = 115$	$l = 150$	$l = 200$
IRAS sources at 30 GHz (μK)	...	19	...	...	...
Radio sources at 30 GHz (μK)	...	16	23	16	13
Radio sources at 40 GHz (μK)	...	11	10	...	
SFD 30 GHz (μK).....	18	...	...	...	...
SFD 40 GHz (μK).....	...	9	...	...	...

NOTE.—A value is not given if the fitted foreground contribution is less than 7 μK. At $l = 60$ this corresponds to a 1% correction and at $l = 200$ a 0.5% correction.

[a] The foreground contribution for a typical value of l.

TABLE 13
SUMMARY OF RESULTS FROM SK, QMAP, AND TOCO

Experiment	l_e[a]	$N_{n\text{-pt}}$[b]	$N_{\rm bins}$[c]	$\delta T_l^{\rm origd}$ (μK)	$\delta T_l^{\rm fce}$ (μK)	$\delta T_l^{\rm f}$ (μK)	δT_l^2 (μK)^2
TOCO.....	63^{+18}_{-18}	2	16, 20	$39.7^{+10.3}_{-6.5}$	35.4	$35.1^{+10.2}_{-6.4}$	1232^{+820}_{-408}
QMAP.....	80^{+41}_{-41}	...	...	47^{+6}_{-7}	46.0	$48.3^{+6.4}_{-7.5}$	2401^{+668}_{-679}
TOCO.....	86^{+16}_{-22}	3	17–28	$45.3^{+7.0}_{-6.4}$	43.4	$43.0^{+6.9}_{-6.3}$	1846^{+644}_{-499}
SK	87^{+39}_{-27}	15	24, 48	49^{+8}_{-5}	48.0	$50.2^{+8.3}_{-5.2}$	2520^{+902}_{-495}
QMAP.....	111^{+64}_{-64}	...	...	52^{+5}_{-5}	52.0	$54.6^{+5.3}_{-5.3}$	3069^{+615}_{-559}
TOCO.....	114^{+20}_{-24}	6	22–42	$70.1^{+6.3}_{-5.8}$	68.0	$67.3^{+6.3}_{-5.8}$	4529^{+888}_{-747}
QMAP.....	126^{+54}_{-54}	...	...	59^{+6}_{-7}	58.0	$60.9^{+6.4}_{-7.5}$	3819^{+832}_{-871}
TOCO.....	128^{+26}_{-33}	1	84	$54.6^{+18.4}_{-16.6}$	54.6	$53.7^{+18.1}_{-16.3}$	2884^{+2272}_{-1485}
TOCO.....	152^{+28}_{-38}	3	84	$82.0^{+11.0}_{-11.0}$	82.0	$80.6^{+10.8}_{-10.8}$	6497^{+1858}_{-1625}
TOCO.....	158^{+22}_{-23}	6	29–55	$88.7^{+7.3}_{-7.2}$	87.2	$86.4^{+7.2}_{-7.1}$	7465^{+1296}_{-1177}
SK	166^{+30}_{-43}	10	48, 96	69^{+7}_{-6}	67.6	$70.5^{+7.3}_{-6.2}$	4970^{+1080}_{-836}
TOCO.....	199^{+38}_{-29}	11	54–82	$84.7^{+7.7}_{-7.6}$	83.7	$82.9^{+7.6}_{-7.6}$	6872^{+1318}_{-1202}
TOCO.....	226^{+37}_{-56}	6	125	$83.0^{+7.0}_{-8.0}$	83.0	$81.6^{+6.9}_{-7.9}$	6659^{+1174}_{-1094}
SK	237^{+29}_{-41}	4	48, 96	85^{+10}_{-8}	83.3	$86.8^{+10.4}_{-8.3}$	7535^{+1914}_{-1372}
SK	286^{+24}_{-36}	4	48, 96	86^{+12}_{-10}	84.3	$87.9^{+12.5}_{-10.4}$	7726^{+2354}_{-1720}
TOCO.....	306^{+44}_{-59}	6	165	$70.0^{+10.0}_{-11.0}$	70.0	$68.8^{+9.8}_{-10.8}$	4733^{+1445}_{-1369}
SK	349^{+44}_{-41}	5	48, 96	69^{+19}_{-28}	67.6	$70.4^{+19.8}_{-29.1}$	4956^{+3180}_{-3275}
TOCO[g]	409^{+42}_{-65}	9	250	<67 (95% conf)	...	$23.3^{+22.4}_{-22.4}$	545 ± 2043

[a] l_e is computed from the window function or the Knox filter following Bond 1995. In practice, there is little difference between the combined weighted windows (Netterfield et al. 1997) and Knox filters (Knox 1999).

[b] The total number of individual n-pt functions combined in the covariance matrix $\boldsymbol{M}$. All known correlations are accounted for. For QMAP, n-pt functions correspond to different eigenmodes for the map.

[c] The number of data points or R.A. bins. When two numbers or a range are given, not all n-pt beams have the same R.A. bins.

[d] The originally published values following the convention in Netterfield et al. 1997. Calibration error is not included.

[e] The original value corrected for foreground emission (fc). For SK, de Oliveira–Costa et al. 1997 found an $\approx$2% contamination of the data due to a foreground component correlated with dust emission. For QMAP a similar correction was found (de Oliveira–Costa et al. 1999). The entries show the spectrum after the corrections. The corrections are done separately for Ka and Q bands before they are combined.

[f] The foreground- and calibration-corrected values. The recalibration is based on new information about the calibration sources or, in the case of TOCO, on a 1%–2% correction for the electronic bandpass. After SK data were published, Mason et al. 1999 reported a more accurate calibration of Cas A. This led to an increase of 4% for the SK data and a reduction in the calibration error from 14% to 10%. There is also a small correction to put the results in the $l(l+1)/2\pi$ format as opposed to the $l(2l+1)/4\pi$. Calibration uncertainty is not included.

[g] Originally, the 95% upper limit and likelihood curves were given for this bin, whereas 1 σ error bars were plotted for the other points. We here adopt the convention by Mauskopf et al. 2000 and give all results with 1 σ error bars. The data are the same as before (Miller et al. 1999) except for the 1.7% calibration correction. The likelihood distribution is not Gaussian. The value of 23 ± 22 μK matches the distribution in the sense that the likelihood peak is at 23 μK and $\approx$95% of the probability is less than $67 = 23 + 2\,\sigma$ μK. The value of 545 ± 2043 (μK)^2 comes from fits to the likelihood following Bond et al. 2000 and is often used to represent the likelihood. Note that $(545 + 2\,\sigma)^{1/2} = 68$ μK. The error bar on δT_l is found by forming $[(545 + 2\,\sigma)^{1/2} - (545)^{1/2}]/2$ μK. For detailed analyses, the full likelihood as shown in Fig. 9 should be used.

a peak could be claimed: $\delta T_{226} > \delta T_{409}$, and $\delta T_{306} > \delta T_{409}$ but with $\delta T_{409} \leq \delta T_{226}$. The net probability that a peak has been detected is given by the sum of the probabilities of these two possibilities.

A Monte Carlo is made of the likelihood distributions to determine the above probabilities and to investigate the effects of correlations. It is found that $P(\delta T_{226} > \delta T_{409}) = 0.99614$ and $P(\delta T_{306} > \delta T_{409} | \delta T_{409} \leq \delta T_{226}) = 0.00369$. Thus, the net probability that a peak has been detected is 0.99983, or loosely speaking, a greater than 3.7 σ detection. The correlations between these three points are positive and small, of order 0.01. When the correlations are accounted for, the net effect is to increase the significance of a detection of a peak. The detection is model independent, calibration independent, and conservative in the sense that if there is slight contamination by point sources or there is some undetected source of correlation, the probability of detection increases. A simple way to assess the probability of a peak detection is to find the net probability that δT_{409} and δT_{306} are less than $\delta T = 82$ μK, the maximum of the δT_{226} distribution. The result is also 0.9998. Another way is just to count the number of σ below $\delta T = 82$ μK.

There are now many analyses that extract cosmological parameters assuming that the models from CMBFAST (Seljak & Zaldarriaga 1996, 1998[37]) describe nature (e.g., Bartlett et al. 1998; Lineweaver 1999; Tegmark & Zaldarriaga 2000; Jaffe et al. 2001). Here we compute $\delta T_{\rm peak}$ and $l_{\rm peak}$ directly from the data. This allows parameter

[37] The CMBFAST code is available through http://physics.nyu.edu/matiasz/CMBFAST/cmbfast.html.

estimation with the minimal amount of model dependence. From the TOCO and SK data, the average amplitude of the peak between $l = 160$ and 240 is $\delta T_{\rm peak} = 80.9 \pm 3.4 \pm 5.1$ μK, where the first uncertainty is statistical and the second uncertainty is for calibration (the 1 μK shift from Miller et al. 1999 is mostly due to the new calibration). Following Knox & Page (2000), it is found that $l_{\rm peak} = 216 \pm 14$ in a relatively model-independent way, as shown in Figure 11.[38]

The SK, QMAP, and TOCO experiments used a variety of techniques, separate data reduction and analysis pipelines, and two different calibrators. These different experiments, rich with consistency checks, trace out a peak. The systematic checks, focusing on the TOCO data, have been described, and no instrumental effect or data reduction artifact that could mimic or produce the signal was found. It is possible that extragalactic sources with spectra different from the ones assumed could alter our results, but the effect would be small and accounting for it would tend to enhance the downturn for $l > 220$. In conclusion, these experiments, in particular the TOCO experiment, have measured the rise, amplitude, position, and fall of the first peak in the angular spectrum of the CMB.

The QMAP and TOCO experiments took place over 6 years and involved many colleagues. We gratefully acknowledge conversations with and help from Chuck Bennett, Joe Fowler, Lloyd Knox, Steve Meyer, Steve Myers, Bharat Ratra, David Spergel, Suzanne Staggs, Dave Wilkinson, and Bruce Winstein. The TOCO and QMAP experiments made ample use of the insights and previous efforts of Norm Jarosik and Ed Wollack. As just one example, Norm's electronics have worked flawlessly for 6 years. Max Tegmark and Angelica de Oliveira–Costa led the science analysis of the QMAP data and have had a large influence on the work presented here. The Princeton Machine Shop time and again came up with rapid and creative solutions to our mechanical problems. Operating in Chile would have been considerably more difficult without the kind and frequent help of Angel Otárola. The Cerro Toco site was graciously provided by Hernán Quintana; Ted Griffith and Eugene Ortiz helped in field. Ray Blundell and colleagues loaned us a C-band amp at a critical time. Angela Qualls made figures for this paper and helped the project on innumerable occasions. Harvey Moseley made the connection between time domain beam synthesis and Fourier transform spectroscopy that we note in the paper. Neither experiment would have been possible without NRAO's detector development. Additionally, NRAO's site monitoring was invaluable for assessing Cerro Toco. We thank the NSBF for two wonderful balloon launches. The WOMBAT foreground compilation greatly assisted us in the data analysis. We also thank Lucent Technologies for donating the radar trailer. We gratefully acknowledge comments by an anonymous referee that improved this paper. This work was supported by an NSF NYI award; a Cottrell Award from the Research Corporation; a David and Lucile Packard Fellowship to L. P.; a NASA GSRP fellowship, Dodds Fellowship, and Hubble Fellowship to A. M.; an NSF graduate fellowship to M. N.; a Dicke Fellowship to E. T.; a Sloan Foundation Award and NSF Career award (AST-9732960) to M. D.; NSF grants PHY-9222952, PHY-9600015, and PHY-0099493; NASA grant NAG 5-6034; and University of Pennsylvania. The data on which this paper are based are public and may be found at http://imogen.princeton.edu/mat.

[38] The peak value from this method, $\delta T_{\rm peak} = 86 \pm 8$ μK, is sensitive to the type of fit, whereas $l_{\rm peak}$ is relatively fit independent. The straightforward average is preferred as it is computed directly from the data.

REFERENCES

Baars, J. W. M., Genzel, R., Pauliny-Toth, I. I. K., & Witzel, A. 1977, A&A, 61, 99
Bahcall, N., Ostriker, J. P., Perlmutter, S., & Steinhardt, P. J. 1999, Science, 284, 1481
Baker, J. C., et al. 1999, MNRAS, 308, 1173
Bartlett, J. G., Blanchard, A., Douspis, M., & Le Dour, M. 1998, Proc. Evolution of Large Scale Structure (Garching: ESO)
Blundell, R., Miller, R. E., & Gundlach, K. H. 1992, Int. J. Infrared Millimeter Waves, 13, 1
Bock, J., Glenn, J., Grannan, S., Irwin, K., Lange, A., LeDuc, H., & Turner, A. 1998, Proc. SPIE, 3357, 297
Bond, J. R. 1995, Astrophys. Lett. Commun., 32, 1
———. 1996, in Cosmology and Large-Scale Structure, Les Houches Session LX, Theory and Observations of the Cosmic Microwave Background Radiation, ed. R. Schaeffer (Dordrecht: Elsevier), 7
Bond, J. R., Crittenden, R., Davis, R. L., Efstathiou, G., & Steinhardt, P. J. 1994, Phys. Rev. Lett., 72, 13
Bond, J. R., Jaffe, A. H., & Knox, L. 2000, ApJ, 533, 19
Chini, R., Kreysa, E., Mezger, P. G., & Gemünd, H. P. 1984, A&A, 137, 117
Clarricoats, P. J. B., & Olver, A. D. 1984, Corrugated Horns for Microwave Antennas (London: Peter Peregrinus)
Coble, K., et al. 1999, ApJ, 519, L5
Condon, J. J., Griffith, M. R., & Wright, A. E. 1993, AJ, 106, 1095
Cornish, N. 2001, Phys. Rev. D, 63, 023702
Cortiglioni, S. 1994, Rev. Sci. Instrum., 65, 2667
Cottingham, D. 1987, Ph.D. thesis, Princeton Univ.
de Bernardis, P., et al. 1994, ApJ, 422, L33
———. 2000, Nature, 404, 955
———. 2002, ApJ, 564, 559
de Oliveira-Costa, A., Devlin, M. J., Herbig, T. H., Miller, A. D., Netterfield, C. B., Page, L. A. & Tegmark, M. 1998a, ApJ, 509, L77
de Oliveira–Costa, A., et al. 1999, ApJ, 527, L9
———. 2002, ApJ, 567, 363
de Oliveira–Costa, A., Kogut, A., Devlin, M. J., Netterfield, C. B., Page, L. A., & Wollack, E. J. 1997, ApJ, 482, L17
de Oliveira–Costa, A., Tegmark, M., Page, L. A., & Boughn, S. 1998b, ApJ, 509, L9
Devlin, M. J., de Oliveira–Costa, A., Herbig, T., Miller, A. D., Netterfield, C. B., Page, L. A., & Tegmark, M. 1998, ApJ, 509, L69
Dicke, R. H. 1946, Rev. Sci. Instrum., 17, 268
Dodelson, S., & Knox, L. 2000, Phys. Rev. Lett., 84, 3523
Doroshkevich, A. G., Zeldovich, Ya. B., & Sunyaev, R. 1978, Soviet Astron., 22, 523
Downey, P., et al. 1984, Appl. Opt., 23, 910
Drain, B. T., & Lazarian, A. 1998, ApJ, 494, L19
Fixsen, D., et al. 1996, ApJ, 470, 63
Fixsen, D., Hinshaw, G., Bennett, C. L., & Mather, J. C. 1997, ApJ, 486, 623
Ganga, K., Page, L., Cheng, E., & Meyer, S. 1994, ApJ, 432, L15
Gaustad, J. E., McCullough, P. R., & Van Buren, D. 1996, PASP, 108, 351
Goldin, A., et al. 1997, ApJ, 488, L161
Griffin, M. J., Ade, A. R., Orton, G. S., Robson, E. I., Gear, W. K., Nolt, I. G., & Radostitz, J. V. 1986, Icarus, 65, 244
Griffith, M. R., & Wright, A. E. 1993, AJ, 105, 1666
Gundersen, J., et al. 1995, ApJ, 443, L57
Haffner, L. M., Reynolds, R. J., & Tufte, S. L. 1999, ApJ, 523, 223
Halverson, N., et al. 2002, ApJ, 568, 38
Hanany, S., et al. 2000, ApJ, 545, L5
Hancock, S., Davies, R. D., Lasenby, A. N., Guiterrez de La Cruz, C. M., Watson, R. A., Rebolo, R., & Beckman, J. E. 1994, Nature, 367, 333
Harrison, D. L., et al. 2000, MNRAS, 316, L24
Haslam, C. G. T., Stoffel, H., Salter, C. J., & Wilson, W. E. 1982, A&AS, 47, 1
Herbig, T., Devlin, M. J., de Oliveira–Costa, A., Miller, A. D., Page, L. A., & Tegmark, M. 1998, ApJ, 509, L73
Hivon, E., Gorski, K. M., Netterfield, C. B., Crill, B. P., Prunet, S., & Hansen, F. 2002, ApJ, 567, 2
Hobson, M. P., Lasenby, A. N., & Jones, M. 1995, MNRAS, 275, 863
Jaffe, A., et al. 2001, Phys. Rev. Lett., 86, 3475
James, G. L., & Thomas, B. M. A. 1982, IEEE Trans. Microwave Theory Tech., MTT-30, 3, 278

Jarosik, N. 1996, IEEE MTT, 44, 2, 193
Jones, W. C. 1997, Junior paper, Princeton Univ.
Kamionkowski, M., Spergel, D., & Sugiyama, N. 1994, ApJ, 426, L57
Keller, J. 1962, J. Opt. Soc. Am., 52, 116
Kerr, A. R., Feldman, M. J., & Pan, S. K. 1997, in Proc. 8th Internat. Symp. on Space Terahertz Technology, Receiver Noise Temperature, the Quantum Noise Limit, and the Role of the Zero-Point Fluctuations
Kerr, A. R., Pan, S. K., Lichtenberger, A. W., Lloyd, F. L., & Horner, N. 1993, in Proc. 4th Internat. Symp. on Space Terahertz Technology, A New SIS Mixer for the 2 mm Band
Knox, L. 1995, Phys. Rev. D, 52, 4307
———. 1999, Phys. Rev. D, 60, 103516
Knox, L., & Page, L. 2000, Phys. Rev. Lett., 85, 1366
Kogut, A., Banday, A. J., Bennett, C. L., Gorski, K. M., Hinshaw, G., & Reach, W. T. 1996, ApJ, 460, 1
Landau, L. D., & Lifshitz, E. M. 1960, Electrodynamics of Continuous Media (Elmsford: Pergamon)
Lee, A., et al. 2001, ApJ, 561, L1
Lee, A., Richards, P., Nam, S., Cabrera, B., & Irwin, K. 1996, Appl. Phys. Lett., 69, 1801
Leitch, E. M., et al. 2002, ApJ, 568, 28
Leitch, E. M., Readhead, A. C. S., Pearson, T. J., & Myers, S. T. 1997, ApJ, 486, L23
Leitch, E. M., Readhead, A. C. S., Pearson, T. J., Myers, S. T., Gulkis, S., & Lawrence, C. R. 2000, ApJ, 532, 37
Lim, M. A., et al. 1996, ApJ, 469, L69
Lineweaver, C. H. 1999, Science, 284, 1503
Masi, et al. 2001, ApJ, 553, L93
Mason, B. S., Leitch, E. M., Myers, S. T., Cartwright, J. K., & Readhead, A. C. S. 1999, AJ, 118, 2908
Mauskopf, P., et al. 2000, ApJ, 536, L59
Mezger, P. G., Tuffs, R. J., Chini, R., Kreysa, E., & Gemünd, H. P. 1986, A&A, 167, 145
Miller, A., et al. 1999, ApJ, 524, L1
Monnelly, G. P. 1996, Senior thesis, Princeton Univ.
Netterfield, C. B., Devlin, M. J., Jarosik, N., Page, L., & Wollack, E. J. 1997, ApJ, 474, 47
Netterfield, C. B., et al. 2002, ApJ, in press
Netterfield, C. B., Jarosik, N., Page, L., Wilkinson, D., & Wollack, E. J. 1995, ApJ, 445, L69
Padin, S., et al. 2001, ApJ, 549, L1
Page, L. 1999, Proceedings from the Newton Institute's "Structure Formation in the Universe" Conference
Park, C.-G., Park, C., Ratra, B., & Tegmark, M. 2001, ApJ, 556, 582
Partridge, R. B. 1995, 3K: The Cosmic Microwave Background Radiation (Cambridge: Cambridge Univ. Press)
Peterson, J. B., et al. 2000, ApJ, 532, L83
Piacentini, F., et al. 2002, ApJS, 138, 315
Piccirillo, L., & Calisse, P. 1993, ApJ, 411, 529
Pospieszalski, M. W. 1989, Proc. IEEE Microwave Theory Tech., 37, 1340
———. 1992, Proc. IEEE Microwave Theory Tech., MTT-S, 1369
———. 1997, in Microwave Background Anisotropies, ed F. R. Bouchet (Gif-sur-Yvette: Editions Frontières), 23
Pospieszalski, M. W., et al. 1994, IEEE Microwave Theory Tech., MTT-S Digest, 1345
Pryke, C., et al. 2002, ApJ, 568, 46
Puchalla, J. L., et al. 2002, AJ, 123, 1978
Ratra, B., Ganga, K., Stompor, R., Sugiyama, N., de Bernardis, P., & Górski, K. M. 1999a, ApJ, 510, 11
Ratra, B., Ganga, K., Sugiyama, N., Tucker, G. S., Griffin, H. T., Nguyen, J. B., & Peterson, J. B. 1998, ApJ, 505, 8
Ratra, B., Stompor, R., Ganga, K., Rocha, G., Sugiyama, N., & Górski, K. M. 1999b, ApJ, 517, 549
Romeo, G., Ali, S., Femenía, B., Limon, M., Piccirillo, L., Rebolo, R., & Schaefer, R. 2001, ApJ, 548, L1
Ruhl, J. E., Dragovan, M., Platt, S. R., Kovac, J., & Novak, G. 1995, ApJ, 453, L1
Schlegel, D. J., Finkbeiner, D. P., & Davis, M. 1998, ApJ, 500, 525
Seljak, U., & Zaldarriaga, M. 1996, ApJ, 469, 437
———. 1998, CMBFAST Web site
Simonetti, J. H., Dennison, B., & Topansa, G. A. 1996, ApJ, 458, L1
Smoot, G. F., et al. 1992, ApJ, 396, L1
Staren, J., et al. 2000, ApJ, 539, 52
Tegmark, M. 1997, Phys. Rev. D, 56, 4514
Tegmark, M., de Oliveira–Costa, A., Devlin, M., Netterfield, C. B., Page, L., & Wollack, E. 1997, ApJ, 474, L77
Tegmark, M., Eisenstein, D., Hu, W., & de Oliveira–Costa, A. 2000, ApJ, 530, 133
Tegmark, M., & Zaldarriaga, M. 2000, Phys. Rev. Lett., 85, 2240
Thomas, B. 1978, IEEE Trans. Ant. Prop., AP-26, 2
Torbet, E., et al. 1999, ApJ, 521, L79
Tucker, G. S. 1991, Ph.D. thesis, Princeton Univ.
Tucker, G. S., Gush, H. P., Halpern, M., Shinkoda, I., & Towlson, W. 1997, ApJ, 475, L73
Tucker, J., & Feldman, M. J. 1985, Rev. Mod. Phys., 57, 4
Ulich, B. L. 1981, AJ, 86, 1619
Weiss, R. 1980, ARA&A, 18, 489
White, M., Carlstrom, J., Dragovan, M., & Holzapfel, W. 1999, ApJ, 514, 12
Wilson, G. W., et al. 2000, ApJ, 532, 57
Wollack, E. J. 1994, Ph.D. thesis, Princeton Univ.
———. 1995, Rev. Sci. Instrum., 66, 4305
Wollack, E. J., Devlin, M. J., Jarosik, N. J., Netterfield, C. B., Page, L., Wilkinson, D. 1997, ApJ, 476, 440
Wollack, E. J., Jarosik, N., Netterfield, C. B., Page, L., & Wilkinson, D. 1993, ApJ, 419, L49
Wollack, E. J., & Pospieszalski, M. W. 1998, Characteristics of Broad-Band InP Millimeter-Wave Amplifiers for Radiometry, IEEE MTT-S International Microwave Symposium Digest, 669
WOMBAT 2001, Wavelength-Oriented Microwave Background Analysis Team Home Page
Wright, A. E., Griffith, M. R., Burke, B. F., & Ekers, R. D. 1994, ApJS, 91, 111
Xu, Y., Tegmark, M., & de Oliveira–Costa, A. 2002, Phys. Rev. D, 65, 083002
Xu, Y., Tegmark, M., de Oliveira–Costa, A. Devlin, M. J., Herbig, T., Miller, A. D., Netterfield, C. B., & Page, L. 2000, Phys. Rev. D, 63, 103002